Table of contents

1 Introduction

Surface Plasmon is a phenomenon originating from collective oscillations of electrons on the surface of metals and their interaction with light. Today, its most important application is in the field of biosensors, which provide a tool for study of molecular interactions and rapid and sensitive detection of chemical biological species.

Sensors utilizing surface plasmons on planar metal-dielectric interfaces (Surface Plasmon Resonance sensors) have been implemented in various configurations [1-3] and employed in numerous application areas including biomolecular interaction analysis [4], medical diagnostics [5], environmental monitoring [6, 7] and food safety [8]. This technology has been under development for the last two decades.

There are two types of surface plasmons: surface plasmons propagating on planar metal-dielectric interfaces and surface plasmons localized on metallic nanoparticles and structures of sub-micrometer dimensions (localized surface plasmon, LSP)[9].

Surface plasmons localized on metallic nanoparticles have already found various technological [10], [11], and sensing applications including nanoparticle SERS spectroscopy [12], detection labels [13], colorimetric sensors [14], ratiometric sensors [15] as well as applications in medical diagnostics [16-18].

An important approach to biosensing utilizes the fact that the properties of surface plasmons are very sensitive to changes in refractive index in the proximity of the metal-dielectric interface. This is the effect exploited in Surface Plasmon Resonance chemical sensors and biosensors [19]. A layer of receptors on the surface of the sensor binds selectively the detected molecule in solution. The captured molecules change the refractive index profile in the vicinity of the metal-dielectric interface. The resulting change in properties of the surface plasmon is then measured optically and provides direct information about the binding [20].

Biosensor applications of nanoparticles and nanostructures utilising this property of surface plasmons have been demonstrated on spherical particles [14], triangular particles [18, 21], rod-like particles [22-24], nanoshells [25] and nanorings [26]. Their performance has been theoretically analyzed in [27] and [28]. More complex nanostructures have been proposed: nanohole arrays [29, 30] and nanoparticle arrays [31, 32]. These new approaches to biosensing have several interesting properties not found in biosensors with surface plasmons on planar metallic inter-

faces, in particular larger parameter space for optimization of the sensing structures.

This work focuses on Surface Plasmon Resonance sensors utilizing localized surface plasmons on spherical metallic nanoparticles. This work systematically explores the performance of these sensors theoretically in order to gain understanding of the major factors involved and gives experimental verification of the results of theoretical analysis.

1.1   Localized Surface Plasmon

The interaction of light with a metallic nanoparticle can be described by a simplified model (Figure 1). The metallic nanoparticle consists of a negatively charged cloud of free conduction electrons and a positively charged background (the lattice)[31]. The electric field of the incident light exerts a force on the electron cloud, which is displaced, but is being pulled back by the electrostatic force of the positively charged background. The electron cloud thus behaves as a damped linear harmonic oscillator and as such has a resonant frequency. From this we can expect a peak (resonance) to appear in the spectra of different optical quantities [31].
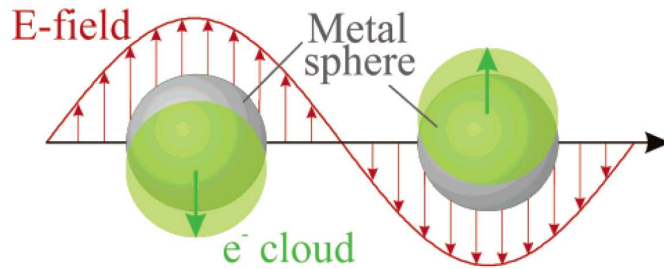
Figure 1: The principle of Localized Surface Plasmon Resonance: conduction electrons and the lattice of a metallic nanosphere as an excited harmonic oscillator (from [31]).

The optical response of an illuminated nanoparticle[1] can be divided into absorption, scattering and extinction. Absorption is due to ohmic losses in the metal. Scattered light is emitted by the oscillations of the electron cloud. Extinction is the summed effect of these two mechanisms on the illuminating beam of light – it describes loss in its intensity. Extinction is straightforwardly measured by measuring transmission; therefore extinction is the property of interest in this work. Scattering can also be measured, for example, in dark-field microscopy [33].

Extinction, scattering and absorption can be characterized by their effective cross-sections. The absorption cross-section is defined as the ratio of the power (W)

---

[1] "Nano" today usually implies quantum effects. Even though this word is used here, optical properties of metallic nanoparticles larger than 10 nm can be described by a classical theory.

absorbed by the particle and the intensity (W/m^2) of the incident light. Similar definitions apply to extinction and scattering cross-sections. The unit of cross-section is m^2.

In an approximation of particles small compared with the wavelength, it can be shown that the extinction cross-section C_{ext} for a particle of permittivity ε_1 in a dielectric medium of permittivity ε_m is [16]

$$C_{ext}(\lambda) \sim \text{Im}\left\{\frac{\varepsilon_1(\lambda) - \varepsilon_m}{\varepsilon_1(\lambda) + 2\varepsilon_m}\right\} \tag{1}$$

At wavelengths for which ε_1 is close to $-2\varepsilon_m$, the denominator will be very small and extinction will have a maximum. This is the peak predicted by the damped oscillator model. When the refractive index (permittivity) of the dielectric medium changes, the wavelength of maximum extinction changes as well. This can be observed in Figure 4, where the extinction spectrum for a 30 nm gold nanoparticle on media of different refractive indices was plotted.
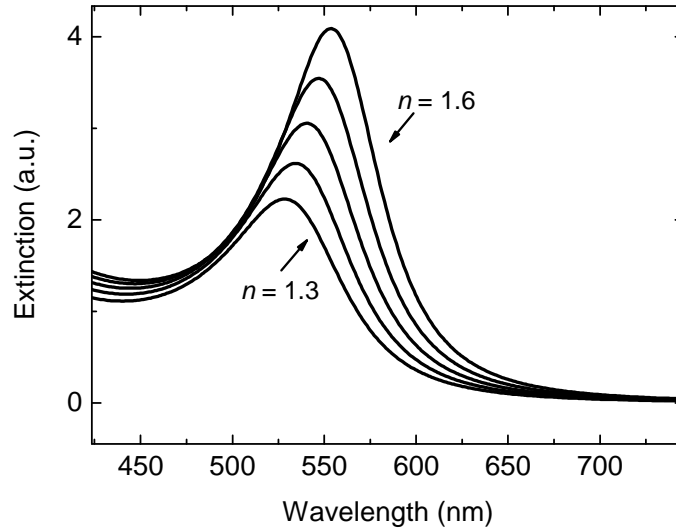
Figure 2: Dependence of extinction spectrum of a 30 nm gold spherical nanoparticle on the refractive index of the medium.

1.2 Biosensors based on LSPs on metallic nanoparticles

The refractive index (RI) change, which induces the shift in maximum of extinction and scattering, can occur either in the volume of the medium or only in the vicinity of the surface of the particle. This effect can be exploited for sensing and biosensing [18].

4

In a sensor based on spectroscopy of LSPs on metallic nanoparticles, the surfaces of the particles are covered with immobilized biorecognition elements. Target molecules are brought into contact with the nanoparticles and specifically bind to the biorecognition elements. This changes the refractive index profile in the vicinity of the surface. Consequently, the extinction (scattering) maximum shifts. This shift can be spectroscopically measured. From the magnitude of the shift the amount of molecules that have bound can be determined [18].
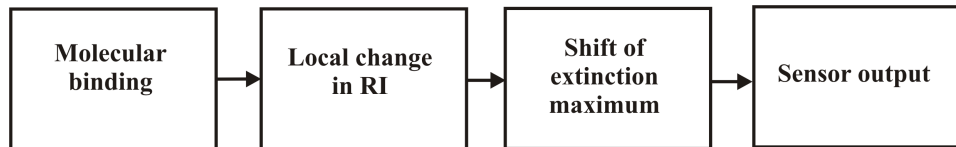
Figure 3: Basic scheme of biosensing with localized surface plasmons.

2   Aim of work

The aim of this work is to explore the potential of localized surface plasmons on metallic nanoparticles as a sensing platform. Optically excited localized surface plasmons are studied both theoretically and experimentally. A set of appropriate modeling tools is selected and described. Both analytical and numerical simulations are pursued to describe, both qualitatively and quantitatively, the phenomenon of optical excitation of surface plasmons on metallic nanoparticles. Optimization of the nanoparticles as a sensing platform with respect to the main design parameters is also performed. Experimental setup for spectroscopic characterization of localized surface plasmons on metallic nanoparticles is established. Selected systems of nanoparticles are investigated in terms of their ability to serve as a high-accuracy refractometric sensors. Ability of the nanoparticle based sensing platform to detect molecular binding events is also demonstrated.

3 Theory

3.1 Electromagnetic Modeling Tools

This section describes the four techniques used in theoretical section of this work. These are:

1. Electrostatic approximation: a simple analytical method, limited to spherical particles small compared with the wavelength,

2. Mie theory: an analytical method, restricted to spherical particles,

3. Discrete Dipole Approximation: a numerical method, limited to isolated particles and

4. Finite Differences in Time Domain: a numerical method allowing arbitrary geometry, but computationally expensive.

3.1.1 Electrostatic approximation

The simplest quantitative model of LSP on a nanoparticle is the electrostatic approximation [16]. Here we suppose that the particle is much smaller than the wavelength of the incident light, so that the field of the incident wave is approximately constant in the vicinity of the particle. The problem of interaction of a nanosphere with light is then reduced to the much simpler problem of a sphere in a homogeneous electric field. The electrostatic theory can also be extended to particles with an overlayer [16].

In this analysis, the electric field of the LSP and the extinction and scattering cross-sections will be calculated.

Let the static, uniform electric field be $\mathbf{E}_0 = E_0 \hat{\mathbf{e}}_z$. The charge induced on the surface of the sphere of permittivity ε_1 and radius a in medium of permittivity ε_m will disturb this field. The electric fields inside and outside of the sphere will be denoted $\mathbf{E}_1$ and $\mathbf{E}_2$ and their potentials $\Phi_1(r,\theta)$ and $\Phi_2(r,\theta)$ (in spherical coordinates r,θ,φ). These potentials satisfy La Place's equation in the regions inside and outside the sphere. On the surface of the sphere, the potential and its derivative weighted by permittivity is required be continuous:

$$\Phi_1 = \Phi_2 \ \text{ and } \ \varepsilon_1 \frac{\partial \Phi_1}{\partial r} = \varepsilon_{\mathrm{m}} \frac{\partial \Phi_2}{\partial r} \ \ (r=a). \tag{2}$$

We also require that $\lim_{r \to \infty} \Phi_2 = -E_0 z$. The first (dipolar) solutions are

$$\Phi_1 = -\frac{3\varepsilon_{\mathrm{m}}}{\varepsilon_1 + 2\varepsilon_{\mathrm{m}}} E_0 r \cos\theta \ , \tag{3}$$

$$\Phi_2 = -E_0 r \cos\theta + a^3 E_0 \frac{\varepsilon_1 - \varepsilon_{\mathrm{m}}}{\varepsilon_1 + 2\varepsilon_{\mathrm{m}}} \frac{\cos\theta}{r^2} \ . \tag{4}$$

Φ_2 is a sum of the incident field and the field of an ideal dipole. The potential of an ideal dipole of dipole moment $\mathbf{p}$ is

$$\Phi = \frac{\mathbf{p} \cdot \mathbf{r}}{4\pi\varepsilon_{\mathrm{m}} r^3} = \frac{p \cos\theta}{4\pi\varepsilon_{\mathrm{m}} r^2} \ . \tag{5}$$

The field generated by the sphere is that of an ideal dipole with a dipole moment of

$$\mathbf{p} = 4\pi\varepsilon_{\mathrm{m}} a^3 \frac{\varepsilon_1 - \varepsilon_{\mathrm{m}}}{\varepsilon_1 + 2\varepsilon_{\mathrm{m}}} \mathbf{E}_0. \tag{6}$$

The sphere behaves as an dipole with polarizability α, which is defined by $\mathbf{p} = \varepsilon_{\mathrm{m}}\alpha\mathbf{E}_0$:

$$\alpha = 4\pi a^3 \frac{\varepsilon_1 - \varepsilon_{\mathrm{m}}}{\varepsilon_1 + 2\varepsilon_{\mathrm{m}}}. \tag{7}$$

From the radiating dipole's polarizability, its extinction and scattering cross-sections can be determined. This is described in [16], chap. 3. For an ideal dipole with polarizability α, the cross-sections for extinction and scattering are

$$C_{\mathrm{ext}} = k \operatorname{Im}\{\alpha\}, \tag{8}$$

$$C_{\mathrm{sca}} = \frac{k^4}{6\pi} |\alpha|^2. \tag{9}$$

where k is the wave-vector size and Im{ } denotes imaginary part of a complex number. Finally, the equations for extinction and scattering cross-sections for sphere small compared with the wavelength are

$$C_{\mathrm{ext}} = 4\pi k a^3 \operatorname{Im}\left\{\frac{\varepsilon_1 - \varepsilon_{\mathrm{m}}}{\varepsilon_1 + 2\varepsilon_{\mathrm{m}}}\right\}, \tag{10}$$

$$C_{\mathrm{sca}} = \frac{8}{3}\pi k^4 a^6 \left|\frac{\varepsilon_1 - \varepsilon_{\mathrm{m}}}{\varepsilon_1 + 2\varepsilon_{\mathrm{m}}}\right|^2. \tag{11}$$

As these equations only apply to small particles, for which scattering is negligible compared with absorption, the equation for C_{ext} is in fact the equation for C_{abs}.

A plot of extinction spectra for particles of different sizes, computed from the electrostatic approximation (thick line) is in Figure 4. Extinction spectra from the Mie theory (which provides exact solution of the same problem) are plotted for

comparison. In this figure, the spectra are normalized to remove the dependence on a^3 described by Equation (10). We can see that the position and shape of the spectrum in electrostatic approximation doesn't change with particle size. The position of the maximum is accurate to within 10 nm for particles of size up to 30 nm and the shape is well described for particles up to about 80 nm.

From Equations (10) and (11) it can be deduced that the values of the cross-sections are high when the denominator of the fraction is small, i.e. if ε_l (metal permittivity) approaches ε_m (permittivity of the medium). The minimum value of the denominator (and maximum value of extinction) depends on the dielectric function of the metal of the particle. For gold, silver and copper, the resulting peak is easily observable in the spectrum, while for most other metals the peak is far less pronounced. [16].
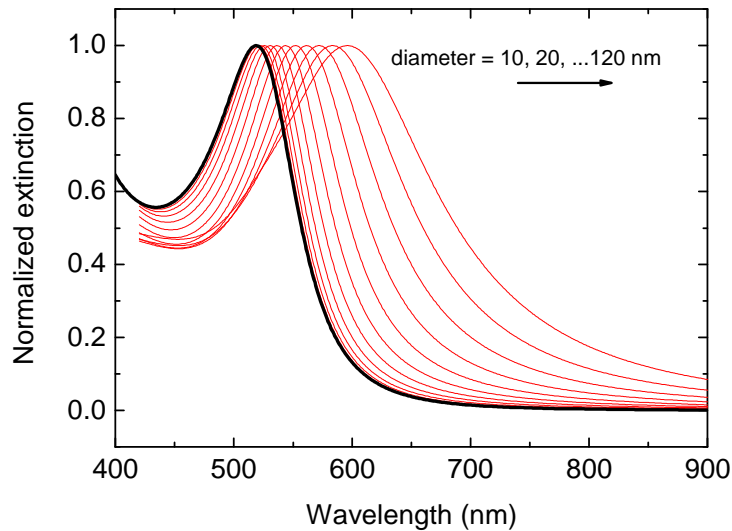
Figure 4: Comparison of extinction cross-section spectra, normalized by their maximum value, for spherical particles as computed by the electrostatic approximation (thick line) and by the Mie theory (thin lines) from 10 to 120 nm diameter in 10 nm increments (without normalization, the spectra would grow with cube of the diameter).

3.1.2 Mie theory

The Mie theory [16] is the exact and complete solution to the problem of scattering and absorption of light by a sphere of arbitrary complex refractive index, with no approximations. It was first published by Gustav Mie in 1908 [34]. The theory is based on expressing the incident plane wave, the scattered and interior electromagnetic (EM) fields as a sum of vector spherical harmonics. The expansion coefficients are then found using the boundary conditions on the sphere's surface (continuity of tangential components). Because now the complete EM field is

known, any quantity of interest, e.g. scattering or extinction cross-section, can be calculated.

The Mie theory can be extended to particles with spherical overlayer. The derivation is nearly identical, only more complicated [16].

Implementation

An implementation of the Mie theory has been written in the Python programming language, see Appendix for the program listing. For computations involving coated particles, a Matlab implementation by C. Mätzler [35] has been used.

Derivation

A detailed derivation of the Mie theory is given in [16]. In the following section, its main points will be described.

Vector spherical harmonics

The vector spherical harmonics $\mathbf{M}(\mathbf{r})$ and $\mathbf{N}(\mathbf{r})$, into which the fields will be expanded, are the solutions of Maxwell's equations in a homogeneous domain and have the form of

$$\mathbf{M} = \nabla \times (\mathbf{r}\psi) \quad \text{and} \quad \mathbf{N} = \frac{\nabla \times \mathbf{M}}{k}, \tag{12}$$

where k is the wave-vector size and ψ is the generating function. The generating function will be selected to satisfy the scalar wave equation $\nabla^2 \psi + k^2 \psi = 0$. With this choice, $\mathbf{M}$ and $\mathbf{N}$ satisfy the vector wave equation and are also divergence-free.

We then solve the scalar wave equation by separation of variables in spherical coordinates. Two sets of generating functions, even and odd, result:

$$\begin{aligned}
\psi_{emn} &= \cos m\varphi P_n^m (\cos\theta) z_n (kr) \\
\psi_{omn} &= \sin m\varphi P_n^m (\cos\theta) z_n (kr)
\end{aligned}, \tag{13}$$

where z_n is any of the four spherical Bessel functions $j_n, y_n, h_n^{(1)}, h_n^{(2)}$, $h_n^{(1)}(\rho) = j_n(\rho) + iy_n(\rho)$, $h_n^{(2)}(\rho) = j_n(\rho) - iy_n(\rho)$ and P_n^m is the associated Legendre polynomial of degree n and order m. Now we have a complete and orthogonal set of basis functions:

$$\begin{aligned}
\mathbf{M}_{emn}^{(i)} &= \nabla \times (\mathbf{r}\psi_{emn}^{(i)}), \quad \mathbf{M}_{omn}^{(i)} = \nabla \times (\mathbf{r}\psi_{omn}^{(i)}) \\
\mathbf{N}_{emn}^{(i)} &= \frac{\nabla \times \mathbf{M}_{emn}^{(i)}}{k}, \qquad \mathbf{N}_{omn}^{(i)} = \frac{\nabla \times \mathbf{M}_{omn}^{(i)}}{k}
\end{aligned}, \tag{14}$$

where i is from 1 to 4 and denotes whether the corresponding function is based on the spherical Bessel function, in the following order: $j_n, y_n, h_n^{(1)}$ or $h_n^{(2)}$.

Incident field

The sphere is illuminated by a plane wave of the form

$$\mathbf{E}_{\mathrm{i}} = \mathbf{E}_0 e^{ikr\cos\theta}\hat{\mathbf{e}}_x. \tag{15}$$

The expansion of the plane wave into vector spherical harmonics can be found in [16], Chapter 4. The result is

$$\mathbf{E}_{\mathrm{i}} = E_0 \sum_{n=1}^{\infty} i^n \frac{2n+1}{n(n+1)} (\mathbf{M}_{\mathrm{o}1n}^{(1)} - i\mathbf{N}_{\mathrm{e}1n}^{(1)}). \tag{16}$$

Internal and Scattered fields

The expansion of the scattered fields has the following form:

$$\mathbf{E}_{\mathrm{s}} = \sum_{n=1}^{\infty} E_n (ia_n \mathbf{N}_{\mathrm{e}1n}^{(3)} - b_n \mathbf{M}_{\mathrm{o}1n}^{(3)})$$
$$\mathbf{H}_{\mathrm{s}} = \frac{k}{\omega\mu} \sum_{n=1}^{\infty} E_n (ib_n \mathbf{N}_{\mathrm{o}1n}^{(3)} + a_n \mathbf{M}_{\mathrm{e}1n}^{(3)}) \tag{17}$$

where E_n is defined to simplify the equations as

$$E_n = i^n E_0 \frac{2n+1}{n(n+1)}. \tag{18}$$

The vector harmonics with the superscript (3) are based on the spherical Hankel functions $h_n^{(1)}(\rho) = j_n(\rho) + iy_n(\rho)$. They were selected because they represent an outgoing spherical wave. The fact that vector harmonics with $m \neq 1$ are not present in the expansion of the incident field requires that these harmonics are not t present in the scattered and internal fields' expansions either.

The internal fields exhibit the following form

$$\mathbf{E}_1 = \sum_{n=1}^{\infty} E_n (c_n \mathbf{N}_{\mathrm{o}1n}^{(1)} - id_n \mathbf{M}_{\mathrm{e}1n}^{(1)})$$
$$\mathbf{H}_1 = \frac{-k_1}{\omega\mu} \sum_{n=1}^{\infty} E_n (d_n \mathbf{N}_{\mathrm{e}1n}^{(1)} + ic_n \mathbf{M}_{\mathrm{o}1n}^{(1)}) \tag{19}$$

The vector harmonics (1) based on the j_n Bessel functions were selected because y_n diverges near 0.

The next step is to determine the expansion coefficients a_n, b_n, c_n, d_n.

Boundary condition and expansion coefficients

The boundary condition that is used to obtain the expansion coefficients is the continuity of tangential field components on the sphere's surface

$$(\mathbf{E}_{\mathrm{i}} + \mathbf{E}_{\mathrm{s}} - \mathbf{E}_1) \times \hat{\mathbf{e}}_{\mathrm{r}} = (\mathbf{H}_{\mathrm{i}} + \mathbf{H}_{\mathrm{s}} - \mathbf{H}_1) \times \hat{\mathbf{e}}_{\mathrm{r}} = 0. \tag{20}$$

When substituting the expansions (16), (17) and (19) into the component form of condition (20) and using the orthogonality of the vector spherical harmonics – equating the left and right hand sides of (20) term-by-term – we obtain four linear

equations for every n. These can be solved yielding equations for a_n, b_n, c_n, d_n. Since for determining the scattering, absorption and extinction cross-sections only the scattered field is needed, only a_n and b_n are shown here:

$$a_n = \frac{m\psi_n(mx)\psi_n'(x) - \psi_n(x)\psi_n'(mx)}{m\psi_n(mx)\xi_n'(x) - \xi_n(x)\psi_n'(mx)} \tag{21}$$

$$b_n = \frac{\psi_n(mx)\psi_n'(x) - m\psi_n(x)\psi_n'(mx)}{\psi_n(mx)\xi_n'(x) - m\xi_n(x)\psi_n'(mx)},$$

with the following definitions: $\psi_n(\rho) = \rho j_n(\rho)$ and $\xi_n(\rho) = \rho h_n^{(1)}(\rho)$ (the Riccati-Bessel functions), m is the relative refractive index of the particle, $m = n_{\text{particle}} / n_{\text{medium}}$ and x is the size factor $x = kr$ where r is the radius of the particle.

Cross-sections

The process of obtaining the extinction and scattering cross-sections from the expansion coefficients is in detail described in [16], Chapter 4 and yields

$$C_{\text{ext}} = \frac{2\pi}{k^2} \sum_{n=1}^{\infty} (2n+1)\,\text{Re}\{a_n + b_n\}, \tag{22}$$

$$C_{\text{sca}} = \frac{2\pi}{k^2} \sum_{n=1}^{\infty} (2n+1)(|a_n|^2 + |b_n|^2). \tag{23}$$

Limits of usability

The cross-sections are expressed as an infinite sum. In numerical evaluation, this sum has to be truncated. More terms are needed for larger particles (in comparison with the wavelength). This sets a limit on the particle size for which the Mie theory is usable without numerical problems. In the visible wavelength range, dielectric particles of several microns in diameter can be computed, in the case of metallic particles roughly one wave-length is the limit [16].

Small particle limit

If only terms with $n = 1$ are taken, then the resulting formulae for cross-sections are identical to those obtained from the electrostatic approximation. This shows that the electrostatic approximation is basically a small-particle limit of the Mie theory.

3.1.3 Discrete Dipole Approximation (DDA)

The Discrete Dipole Approximation is a numerical method for analysis of light scattering on particles of arbitrary shape [36]. It works by first discretizing the particle into a cubic grid of polarizable dipoles, whose polarizablities are computed from the material's dielectric function. Every dipole's polarization is given by the sum of the incident plane wave field and the dipole fields of all other dipoles, which

depend on their polarizations. Then, the self-consistent polarizations for the dipoles are determined.

Implementation

In this work, the DDSCAT 6.1 implementation by Draine and Flatau [37] was used.

Derivation

The polarization induced in the i-th element is (omitting the frequency dependence $e^{i\omega t}$)

$$\mathbf{P}_i = \alpha_i \mathbf{E}_{\text{loc}}(\mathbf{r}_i), \tag{24}$$

where the local electric field $\mathbf{E}_{\text{loc}} = \alpha_i^{-1} \mathbf{P}_i$ is the sum of the incident field and a contribution from all other dipoles in the particle

$$\alpha_i^{-1} \mathbf{P}_i = \mathbf{E}_{\text{inc}}(\mathbf{r}_i) + \mathbf{E}_{\text{dipole}}(\mathbf{r}_i) = \mathbf{E}_0 \exp(i\mathbf{k} \cdot \mathbf{r}_i) - \sum_{j \neq i} \mathbf{A}_{ij} \cdot \mathbf{P}_j. \tag{25}$$

$\mathbf{E}_0$ and $\mathbf{k}$ are amplitude and wave-vector of the incident wave, and the interaction matrix is ($j \neq i$)

$$\mathbf{A}_{ij} \cdot \mathbf{P}_j = \frac{\exp(ikr_{ij})}{r_{ij}^3} \left\{ k^2 \mathbf{r}_{ij} \times (\mathbf{r}_{ij} \times P_j) + \frac{1 - ikr_{ij}}{r_{ij}^2} [r_{ij}^2 \mathbf{P}_j - 3r_{ij}(\mathbf{r}_{ij} \cdot \mathbf{P}_j)] \right\}. \tag{26}$$

Substituting (26) into (25) and rearranging terms we obtain an equation in a form

$$\mathbf{A}' \cdot \mathbf{P} = \mathbf{E}, \tag{27}$$

where $\mathbf{A}'$ is a matrix built from the previous matrix $\mathbf{A}$. For N dipoles, $\mathbf{P}$ and $\mathbf{E}$ are $3N$-dimensional vectors and $\mathbf{A}'$ is a $3N \times 3N$ matrix. By solving these $3N$ complex linear equations the polarization vector $\mathbf{P}$ is obtained and from it the extinction and scattering cross-section can be directly calculated:

$$C_{\text{ext}}(\lambda) = \frac{4\pi k}{|\mathbf{E}_0|^2} \sum_{j=1}^{N} \text{Im}\{\mathbf{E}_{\text{inc}}^* \cdot \mathbf{P}_j\}, \tag{28}$$

$$C_{\text{sca}}(\lambda) = \frac{k^4}{|\mathbf{E}_0|^2} \int dA \left| \sum_{j=1}^{N} [\mathbf{P}_j - \hat{\mathbf{n}}(\hat{\mathbf{n}} \cdot \mathbf{P}_j)] \exp(-ik\hat{\mathbf{n}} \cdot \mathbf{r}_j) \right|^2. \tag{29}$$

Limitations

Although DDA doesn't require large computing resources for small particles (in visible, this is < 100 nm for metallic particles and < 10 μm for dielectric particles), these requirements grow with the square of the particle volume because of the $3N \times 3N$ matrices. This severely limits the methods' usability for plasmonic nanostructures other than isolated particles. For such systems, the FDTD method is more efficient, since its computational complexity grows only linearly with the simulated volume.

3.1.4   Finite Differences in Time Domain (FDTD)

The Finite Differences in Time Domain method (FDTD) directly solves Maxwell's equations by discretizing the electric and magnetic fields and the material constants on a finite rectangular grid and advancing the fields in time by directly using the Maxwell's curl equations [38]. The spatial derivatives are replaced by differences, and, unlike other methods, which suppose harmonic fields with a given frequency (work in the frequency domain), FDTD follows the time evolution of the fields; hence the name. FDTD could be thought of as a "numerical experiment".

The method was first introduced by Yee in 1966 [39], but became widely used only in the last two decades with the availability of powerful enough computers.

Implementation

In this work, the commercial package Lumerical FDTD Solutions from Lumerical, Inc., Canada [40], was used, running on a cluster consisting of 12 nodes, 2.4 GHz CPU and 2 GB RAM each.

Derivation

FDTD solves the Maxwell's curl equations in the form

$$\frac{\partial \mathbf{E}}{\partial t} = \frac{1}{\varepsilon}\nabla\times\mathbf{H} - \frac{\sigma}{\varepsilon}\mathbf{E}$$
$$\frac{\partial \mathbf{H}}{\partial t} = -\frac{1}{\mu}\nabla\times\mathbf{E} - \frac{\sigma^*}{\mu}\mathbf{H} \tag{30}$$

where σ is the electric conductivity, σ^* magnetic conductivity (non-zero only in special cases), ε permittivity and μ permeability of the medium.

Re-writing these in cartesian coordinates, we obtain equations for the time derivatives of all field components, where derivatives will be replaced by finite differences. Let's take H_x as an example. The equation for H_x is

$$\frac{\partial H_x}{\partial t} = \frac{1}{\mu}\cdot\left(\frac{\partial E_y}{\partial z} - \frac{\partial E_z}{\partial y} - \sigma^* H_x\right). \tag{31}$$

The discretization scheme introduced by Yee [39] can be see in Figure 5. The positions at which individual components of the fields are placed in one grid cell are chosen so that central differences can be used for evaluating the spatial derivatives as in the eq. (31) for H_x and the other five equations. For the same reason, E fields are stored for time t while the H fields are stored for time $t+1/2\Delta t$. Using this scheme, we can substitute (31) with

$$\frac{H_x^{n+1/2}(i,j,k) - H_x^{n-1/2}(i,j,k)}{\Delta t} = \frac{1}{\mu(i,j,k)}\cdot\left(\begin{array}{c}\frac{E_y^n(i,j,k+1/2)-E_y^n(i,j,k-1/2)}{\Delta z} \\ -\frac{E_z^n(i,j+1/2,k)-E_z^n(i,j-1/2,k)}{\Delta y} \\ -\sigma^*(i,j,k)\cdot H_x^n(i,j,k)\end{array}\right), \tag{32}$$

where H_x^n, which is not being stored in the Yee grid, is computed as

$$H_x^n = \frac{H_x^{n+1/2} + H_x^{n-1/2}}{2}.$$

(33)

The notation $H_x^n(i,j,k)$ means the value of H_x in timestep n at point $x = i \cdot \Delta x$, $y = j \cdot \Delta y$, $z = k \cdot \Delta z$. By manipulating the expression (32), we arrive at the explicit update expression for H_x:

$$H_x^{n+1/2}(i,j,k) = \left(\frac{1 - \frac{\sigma^*(i,j,k)\Delta t}{2\mu(i,j,k)}}{1 + \frac{\sigma^*(i,j,k)\Delta t}{2\mu(i,j,k)}} \right) H_x^{n-1/2}(i,j,k)$$

$$+ \left(\frac{\frac{\Delta t}{\mu(i,j,k)}}{1 + \frac{\sigma^*(i,j,k)\Delta t}{2\mu(i,j,k)}} \right) \cdot \left(\frac{E_y^n(i,j,k+1/2) - E_y^n(i,j,k-1/2)}{\Delta z} - \frac{E_z^n(i,j+1/2,k) - E_z^n(i,j-1/2,k)}{\Delta y} \right).$$

(34)
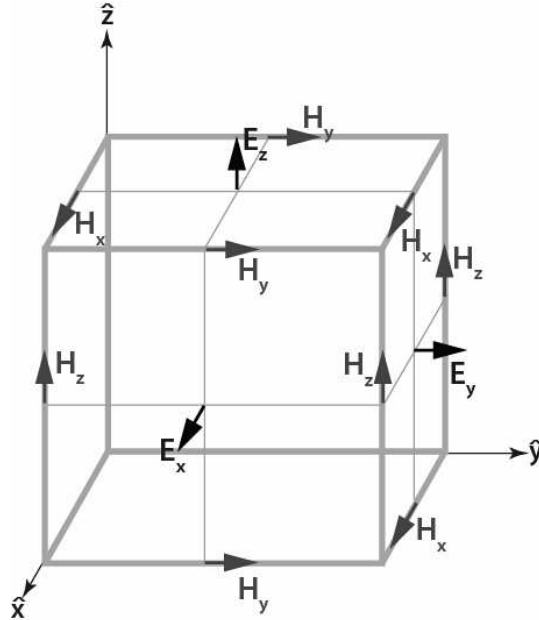
Figure 5: Yee cell, the discretization scheme for FDTD. It is chosen to facilitate the evaluation of the discretized Maxwell's curl equations by central differences. From [38].

The frequency dependence of required quantities can be obtained by discrete Fourier transform from their time dependence as the simulation progresses in time. The cross-sections for absorption and scattering can be computed numerically by integrating the Poynting vector over a surface surrounding the particle. Similarly, other quantities can be computed because complete information about the EM field is available.

Since the area of space which has been discretized is finite, there arises the problem of updating the field values on the edge of the grid. Boundary conditions are needed that would simulate either a closed (e.g. a perfect conductor) or an open boundary

(this corresponds to scattering problems). A boundary condition transparent to outgoing waves, not giving any non-physical reflections was introduced as the Perfectly Matched Layer in 1994 by Berenger [41] and allowed the expansion of FDTD to scattering problems.

Advantages

The main advantage of FDTD over frequency domain methods is that from a single simulation with a broadband pulse it is possible to get the frequency response for the whole spectrum by Fourier transform. The system's response to a pulse can be also obtained (in frequency domain methods, it would be necessary to synthesize it by inverse Fourier transform from a set of harmonic solutions). The FDTD method also allows the use of periodic boundary condition (useful for simulating arrays of particles or photonic crystals).

Another advantage is that the computational time grows only linearly with volume of the simulated area, while in some other methods including DDA this growth is quadratic.

Disadvantages

The FDTD method requires large amounts of memory and processing power, especially for 3D simulations. For simulating a single metallic nanoparticle of 200 nm size, a single workstation with 2 GB of RAM is sufficient; for larger problems, PC clusters are often used.

3.2   Sensitivity of sensors based on LSPs on nanoparticles

In this section, the methods introduced in the previous section will be used to analyze the ability of metallic nanoparticles to serve as LSP based sensors and measure small changes in refractive index. Specifically, analytical results based on the electrostatic approximation and numerical results based on Mie theory, DDA and FDTD will be presented. These results have been also submitted for publication [42].

There are several factors influencing the ability of LSP based sensors to resolve small changes in refractive index. Sensitivity of the LSP based sensor can be defined as a ratio of the change in the wavelength of maximum extinction λ_{peak} and the refractive index change that induced the change in λ_{peak}. Depending on the spatial distribution of the refractive index change, sensitivity for two important limiting cases can be defined. Bulk refractive index sensitivity S_{B} defines sensitivity of changes in the refractive index which occur homogeneously in the whole medium surrounding the particle. Surface refractive index sensitivity is defined as sensitivity to refractive index changes occurring within a thin layer at the surface of the particle. Mathematically, the sensitivities can be expressed as

$$S_{\mathrm{B}} = \frac{\mathrm{d}\lambda_{\mathrm{peak}}}{\mathrm{d}n_{\mathrm{medium}}} \quad \text{and} \quad S_{\mathrm{S}} = \frac{\mathrm{d}\lambda_{\mathrm{peak}}}{\mathrm{d}n_{\mathrm{layer}}} \quad , \tag{35}$$

where n_{layer} denotes the refractive index of the thin layer.

3.2.1 Relation of LSP eigenfrequency to peak wavelength

Localized Surface Plasmon can be described as a mode of the EM field localized on the metallic nanoparticle. Since the particle material is lossy and this mode is radiative (scattering cross-section is non-zero), the eigenfrequency ω_{res} of this mode is complex. The eigenfrequency can be determined from equations for C_{ext} (10) and C_{sca} (11). It is the frequency for which they diverge, i.e. the value of the denominator $\varepsilon_1(\omega) + 2\varepsilon_{\mathrm{m}}$ is zero[2]. Thus the condition for resonant excitation of the LSP in electrostatic approximation is

$$\varepsilon_1(\omega_{\mathrm{res}}) = -2\varepsilon_{\mathrm{m}}. \tag{36}$$

Excitation of the LSP at a frequency close to its eigenfrequency is called the Localized Surface Plasmon Resonance. The complex eigenfrequency ω_{res} is related to the real frequency ω_{peak} for which a peak (maximum) in extinction and scattering can be experimentally observed. Any shift of the complex pole ω_{res} (due to change in ε_{m}) is accompanied by a shift of the maximum ω_{peak}. If ω_{res} lies close to the real axis, then

$$\mathrm{d}\omega_{\mathrm{peak}} = \mathrm{Re}\{\mathrm{d}\omega_{\mathrm{res}}\}, \tag{37}$$

because of properties of $\varepsilon_1(\omega)$. In reality, the imaginary part of ω_{res} is comparable with the real part. If we accept (37) as an approximation, then changes in ω_{peak} (which can be correlated with experiment), can be analyzed by analyzing changes in ω_{res} (which can be done analytically).

In the following text, instead of peak frequency ω_{peak}, peak wavelength $\lambda_{\mathrm{peak}} = 2\pi c / \omega_{\mathrm{peak}}$ will be used, since wavelength is used more in optics. For convenience, resonant frequency (eigenfrequency) ω_{res} will also be replaced by resonant wavelength λ_{res} with the same definition, even though complex wavelength is not often used in literature.

3.2.2 Bulk refractive index sensitivity

Sensitivity of the *resonant* wavelength to a change in refractive index of the medium can be obtained by differentiating the resonance condition (36):

---

[2] Metal permittivity for complex ω is a valid quantity, because it is defined using the impulse response function of the metal in the same way as permittivity for real ω is defined.

$$\frac{d\lambda_{\text{res}}}{dn_{\text{m}}} = \frac{d\lambda_{\text{res}}}{d\varepsilon_{\text{m}}}\frac{d\varepsilon_{\text{m}}}{dn_{\text{m}}} = -\frac{4}{\frac{d\varepsilon_{\text{l}}}{d\lambda}}n_{\text{m}}, \tag{38}$$

where ε_{l} is the metal permittivity and ε_{m} and n_{m} is the permittivity and refractive index of the medium. Using (37), the bulk RI sensitivity S_{B} of the *peak* wavelength to a change in refractive index of the medium is

$$S_{\text{B}} = \text{Re}\left\{\frac{d\lambda_{\text{res}}}{dn_{\text{m}}}\right\} = -\frac{4}{\frac{d\varepsilon_{\text{l}}'}{d\lambda}}n_{\text{m}}, \tag{39}$$

where ε_{l}' denotes the real part of metal permittivity: $\varepsilon_{\text{l}} = \varepsilon_{\text{l}}' + i\varepsilon_{\text{l}}''$. As follows from (39), the main factor which influences the bulk RI sensitivity is the derivative of the real part of the particle's dielectric function.

In Table 1, bulk RI sensitivity for a particle surrounded by a dielectric with a refractive index $n_{\text{m}} = 1.33$ has been computed by three different methods: 1. by Mie thoery, 2. by computing extinction spectra using eq. (10) and determining the sensitivity from them and 3. by eq. (39). Clearly, the electrostatic approximation holds only for small particles (diameter < 30 nm). With increasing particle size, the bulk RI sensitivity also increases as illustrated in Figure 6 which presents sensitivity data obtained from extinction spectra calculated by the Mie theory.

	Bulk RI sensitivity $S_{\text{B}} = d\lambda_{\text{peak}}/dn_{\text{medium}}$		
Diameter (nm)	Mie theory	El.stat. (10)	El.stat. (39)
16	85	81	95
30	93	81	95
80	159	81	95

Table 1: Bulk RI sensitivity for a spherical gold particle in a medium of refractive index of 1.33 computed by Mie theory, by determining the sensitivity from spectra obtained from (10) and by eq. (39).
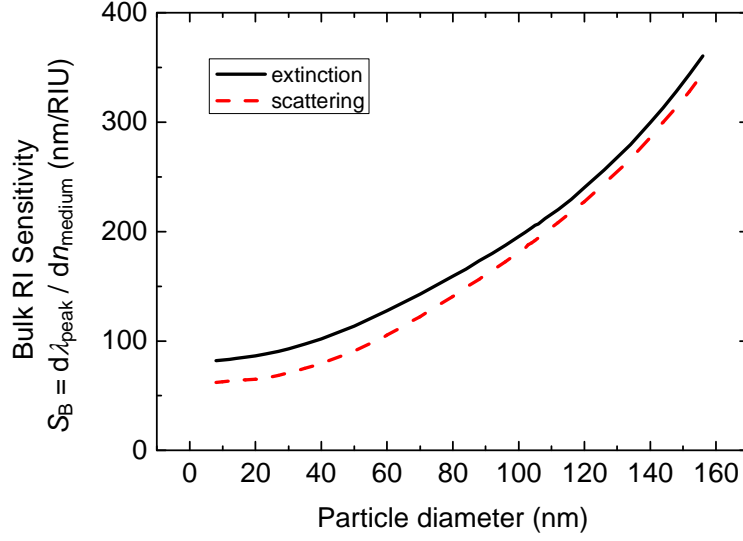
Figure 6. Bulk RI sensitivity of a spherical gold nanoparticle in a medium of refractive index of 1.33 as a function of its diameter, computed by Mie theory.

3.2.3 Surface refractive index sensitivity

In the electrostatic approximation, extinction cross-section of a coated sphere is [16]

$$C_{ext} = \frac{8\pi^2}{\lambda} a_2^3 \, \text{Im}\left\{\frac{(\varepsilon_2 - \varepsilon_m)(\varepsilon_1 + 2\varepsilon_2) + (1-\Delta)(\varepsilon_1 - \varepsilon_2)(\varepsilon_m + 2\varepsilon_2)}{(\varepsilon_2 + 2\varepsilon_m)(\varepsilon_1 + 2\varepsilon_2) + 2(1-\Delta)(\varepsilon_2 - \varepsilon_m)(\varepsilon_1 - \varepsilon_2)}\right\},$$

$$\left(\Delta = 1 - \frac{r^3}{(r+t)^3}\right)$$

(40)

where ε_1 and r denote permittivity and radius of the particle and ε_2 and t denote the permittivity and the thickness of the dielectric layer and Im{ } denotes imaginary part of a complex number. Δ is the volume fraction of the layer versus the entire particle. For a layer of zero thickness $\Delta = 0$ and for infinite thickness $\Delta = 1$. The pole of $C_{ext}(\lambda)$ occurs at the zero of the denominator. The value of ε_1 for which the denominator is equal to zero is:

$$\varepsilon_1 = \frac{2\Delta(\varepsilon_m - \varepsilon_2) - 6\varepsilon_m}{2\Delta(\frac{\varepsilon_m}{\varepsilon_2} - 1) + 3}.$$

(41)

This is the resonance condition for a coated particle, similar to the resonance condition (36) for uncoated particle. The sensitivity can be obtained by differentiation, as in the previous section. If we assume a small increase of permittivity within the layer $\varepsilon_2 \to \varepsilon_2 + d\varepsilon_2$, the corresponding change $\varepsilon_1 \to \varepsilon_1 + d\varepsilon_1$ required for the system to stay at the resonance (pole) can be obtained by differentiating Equation (41):

$$d\varepsilon_1 = d\varepsilon_2 \left[\frac{-2\Delta}{2\Delta(\frac{\varepsilon_m}{\varepsilon_2} - 1) + 3} + \frac{2\Delta(\varepsilon_m - \varepsilon_2) - 6\varepsilon_m}{(2\Delta(\frac{\varepsilon_m}{\varepsilon_2} - 1) + 3)^2} 2\Delta \frac{\varepsilon_m}{\varepsilon_2^2} \right]. \tag{42}$$

If we assume a layer with a refractive index close to that of the background $(\varepsilon_2 - \varepsilon_m) \ll \varepsilon_2$, then (42) can be simplified to

$$d\varepsilon_1 = -2\Delta d\varepsilon_2, \tag{43}$$

and the surface RI sensitivity of *resonant* wavelength can be expressed as:

$$\frac{d\lambda_{res}}{dn_2} = -\frac{4}{\frac{d\varepsilon_1}{d\lambda}} n_2 \Delta. \tag{44}$$

Using (37), the surface RI sensitivity S_S of the *peak* wavelength to a change in RI of the layer is

$$S_S = \mathrm{Re} \left\{ \frac{d\lambda_{res}}{dn_2} \right\} = -\frac{4}{\frac{d\varepsilon_1'}{d\lambda}} n_2 \Delta \tag{45}$$

For very thin layers $(t \ll r)$ the volume fraction Δ can be approximated by $3t / (r + 3t)$. Comparing (45) to eq. (39) for S_B, we see that

$$S_S = S_B \Delta, \tag{46}$$

since we have assumed $n_2 \doteq n_m$. In the approximation of sparse layer, the surface RI sensitivity is basically equal to the bulk RI sensitivity times a factor corresponding to how much of the total "field volume" the layer takes up. As follows from eq. (45), for a fixed layer thickness, larger particles exhibit lower surface refractive index sensitivity. However, this effect is partly compensated by the general increase in sensitivity with an increasing particle size (Figure 6), which was observed for bulk RI sensitivity. This increase is not captured by the electrostatic approximation used to derive equation (45).

To compare analytical results for surface refractive index sensitivity with other approaches, surface sensitivity of gold particles with dielectric overlayer in medium of $n_m = 1.33$ was calculated for different sizes and layer thicknesses using different methods. For comparison, see Table 2.

Surface sensitivity $S_S = d\lambda_{peak} / dn_2$							
Diameter (nm)	Layer (nm)	A: Mie Theory	B: El. stat. (40)	C: El. stat. (45)	D: $S_{B,Mie} \cdot \Delta$	E: FDTD	F: DDA
16	3	51	50	43	52	55	49
30	5	51	46	39	54	51	48
80	5	40	23	19	47	34	31

Table 2. Surface refractive index sensitivity for spherical gold particles with a thin overlayer calculated for three different diameters and overlayer thicknesses using Mie theory, electrostatic approximation (eq. (40)), electrostatic approximation for

sparse thin overlayers (eq. (45)), eq. (46) using bulk sensitivity from Mie theory, by FDTD and by DDA.

In Table 2, letters A to F represent the following:

A: S_S obtained from extinction spectra computed by Mie theory,

B: S_S obtained from extinction spectra computed by electrostatic approximation (eq. (40)), i.e. without further approximations leading to eq. (45),

C: S_S obtained from eq. (45) (sparse layer approximation),

D: S_S obtained from eq. (46), but using the value of S_B obtained from Mie theory (Table 1).

E: S_S obtained from extinction spectra computed by FDTD,

F: S_S obtained from extinction spectra computed by DDA.

As follows from Table 2, there is a good agreement between the electrostatic approximation (Equation (40)) and Mie theory for smaller particles. With increasing particle size, the electrostatic approximation increasingly underestimates the sensitivity and for particles of a diameter of 80 nm (which clearly cannot be described by the electrostatic approximation) predicts sensitivity smaller than that determined by using Mie theory by a factor of almost 2. Column D shows that this discrepancy is due to the inability of the electrostatic approximation to describe effects of increasing particle size. The dependence on Δ is still valid even for larger particles.

Dependence of the surface sensitivity on particle size computed by the Mie theory is presented in Figure 7. Clearly, for very thin layers (thickness – 2 nm), the surface refractive index sensitivity decreases with an increasing particle size for particle diameters up to about 80 nm and then slowly increases with an increasing particle size. Surface sensitivity for systems including thicker overlayers follow the same trend; however the initial decrees for smaller particles is less pronounced and the sensitivity starts to grow for smaller particles and the growth with the increasing particle size is faster (Figure 7). For layers of thickness > 20 nm, the sensitivity monotonically increases with particle size.

Numerical evaluation of equations for S_B (39) and S_S (45) requires the knowledge of $d\varepsilon_1' / d\lambda$ at complex λ_{res} at which the derivative is meant to be taken. This value is not available from experimental data. In the data presented in tables 1 and 2, the value of this derivative at the peak wavelength λ_{peak} was used instead. This fact also contributed to the discrepancy between the results equations for S_B (39) and S_S (45) and other, more accurate methods. But, these expressions serve to provide insight and not exact numerical values.
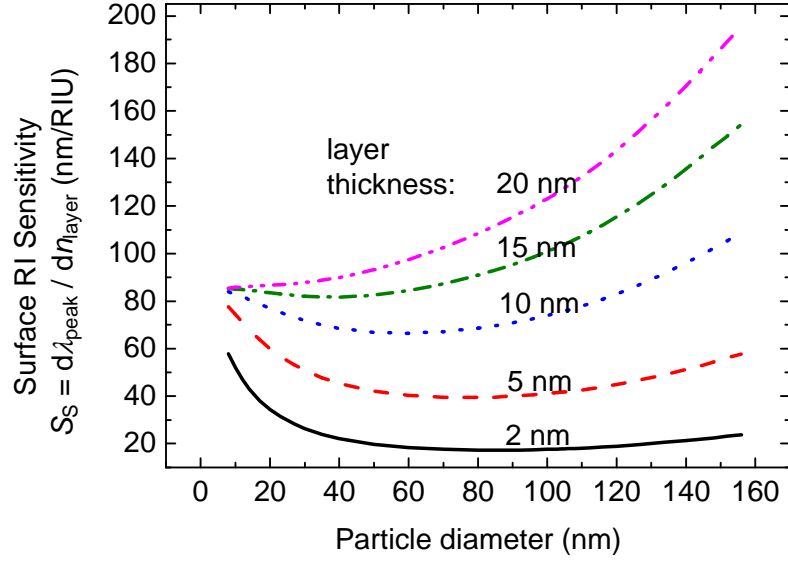
Figure 7: Surface refractive index sensitivity for a gold particle as a function of its diameter calculated for five different thicknesses of the dielectric overlayer using the Mie theory.

As follows from Figure 7, surface sensitivity increases with increasing thickness of the overlayer to become equal to bulk refractive index sensitivity. In order to achieve 50 per cent value of the bulk refractive index sensitivity, the volume fraction Δ needs to be equal to 0.5 which determines the thickness of the overlayer $t_{50} = 0.25r$.

3.2.4   Figure of merit

As illustrated in [20], ability of SPR sensors to resolve small refractive index changes is directly proportional to refractive index sensitivity and indirectly proportional to the width of the resonant feature:

$$\text{resolution} \sim \frac{S}{w} , \qquad (47)$$

where is w width of the peak. In order to evaluate various sensing schemes with respect to their actual sensing potential we introduce the figure of merit χ defined as

$$\chi = \frac{S}{w} , \qquad (48)$$

where S is sensitivity and w is width of the extinction peak (or transmission dip).

As the extinction peak is rather asymmetric, in this work we shall calculate the width of the peak by approximating the vicinity of the maximum by a Lorentzian profile and use the FWHM (full width at half maximum) of this Lorentzian.

Width of the extinction peak

In the electrostatic approximation, eq. (10) can be rewritten as

$$C_{\text{ext}} = \frac{8\pi^2}{\lambda} r^3 \frac{3\varepsilon_1'' \varepsilon_{\text{m}}}{(\varepsilon_1' + 2\varepsilon_{\text{m}})^2 + \varepsilon_1''^2} \ , \tag{49}$$

where $\varepsilon_1 = \varepsilon_1' + i\varepsilon_1''$. In order to obtain approximate width of the extinction peak, we expand C_{ext} into Taylor series around the peak wavelength λ_{peak}, neglect higher order terms, and approximate the imaginary part of permittivity around λ_{peak} by a constant. This yields for C_{ext}

$$C_{\text{ext}} = \frac{8\pi^2}{\lambda} r^3 \frac{3\varepsilon_1''(\lambda_{\text{peak}}) \varepsilon_{\text{m}}}{\left(\left. \frac{d\varepsilon_1'}{d\lambda} \right|_{\lambda_{\text{peak}}} (\lambda - \lambda_{\text{peak}}) \right)^2 + (\varepsilon_1''(\lambda_{\text{peak}}))^2} \tag{50}$$

which has a form of a Lorentzian curve near λ_{peak} with a FWHM equal to

$$w = \frac{2\varepsilon_1''(\lambda_{\text{peak}})}{\left. \frac{d\varepsilon_1'}{d\lambda} \right|_{\lambda_{\text{peak}}}}. \tag{51}$$

Similarly to the sensitivity, the width of the resonant extinction feature depends on the derivative of the real part of the particle's dielectric function, but also on the value of the imaginary. By combining eq. (39) for S_{B} and (51) for w, we obtain

$$\chi_{\text{B}} = \frac{S_{\text{B}}}{w} = -\frac{2}{\varepsilon_1''(\lambda_{\text{peak}})} n_{\text{m}}. \tag{52}$$

Clearly, the figure of merit does not depend on the derivative of the real part of the dielectric function, but only on its imaginary part. This suggests that the use of metal with smaller losses will lead to sensors with potentially better performance.

The width of the extinction feature for large particles cannot be calculated by the electrostatic approximation and has to be determined from Mie theory. As follows from Figure 8, the width of the extinction feature for gold spherical particles remains approximately constant for particle diameter up to about 80 nm and then increases rapidly with increasing particle diameter due to radiative losses.
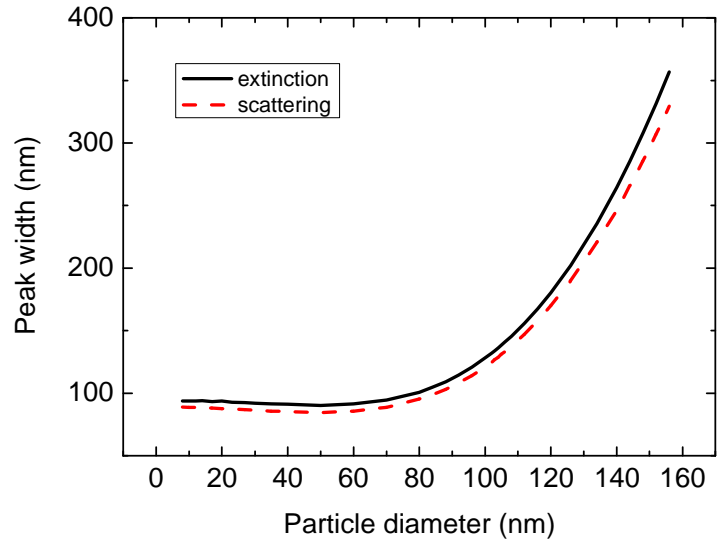
Figure 8. Width of the extinction feature as a function of particle diameter determined by Mie theory.

Figures of merit of bulk and surface sensitivity are shown in Figure 9 and Figure 10, respectively. As follows from Figure 9, performance of refractive index LSPR sensors based on spherical gold particles may vary substantially depending on the size of the used particle. This calculations suggest that for refractometry, the diameter of the particles giving the best performance is around 80 nm.

Dependence of a LSP biosensor performance on the size of the particles may be more complex and will depend also on the thickness of the overlayer within which the refractive index change occurs. From Figure 10 it can be seen that for layers of thickness up to 10 nm, smallest particles provide show highest figure of merit. The actual choice would be influenced by the fact that in particles of diameter less than 10 nm the extinction peak broadens due to limited electron free pathlength [9]. For layers thicker then 10 nm, optimal particle diameter is in the range 80—100 nm.
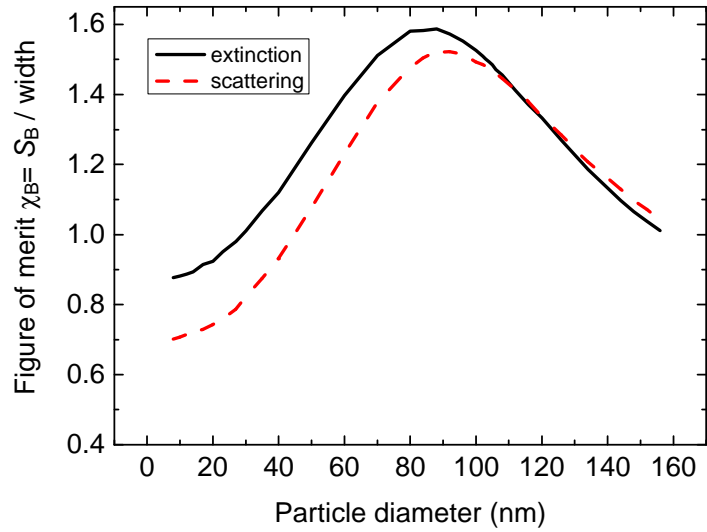
Figure 9. Figure of merit for bulk RI sensitivity (ratio of bulk RI sensitivity to peak width). This takes into account the influence of peak width on sensor resolution. For larger (> 40 nm diameter) particles radiative damping leads to peak broadening which decreases the figure of merit despite the sensitivity still increasing for larger particles. Compare with Figure 6.
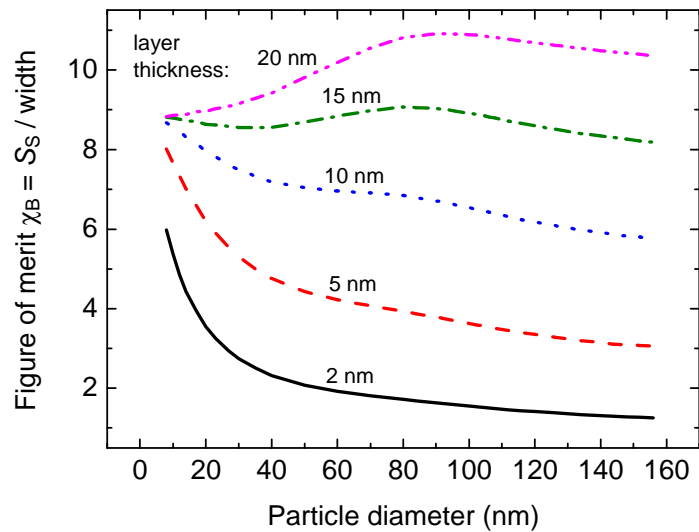
Figure 10. Figure of merit for surface RI sensitivity (ratio of surface RI sensitivity to peak width). for different thicknesses of the overlayer. This takes into account the influence of peak width on sensor resolution. For larger (> 40 nm diameter) particles radiative damping leads to peak broadening which decreases the figure of merit despite the sensitivity still increasing for larger particles. Compare with Figure 7.

3.2.5 Sensitivity of LSPs on non-spherical particles

The electrostatic approximation can be extended to treat spheroidal particles [16]. The main difference is that the resonance condition $\varepsilon_1 + 2\varepsilon_m = 0$, from which the bulk refractive index sensitivity is obtained, changes to $\varepsilon_1 + L\varepsilon_m = 0$, where the shape factor L increases with particle aspect ratio ($L = 2$ for a sphere, $L = 12$ for a 4:1 aspect ratio spheroid [16]). This translates to a corresponding increase in bulk RI sensitivity:

$$S_B = -\frac{2L}{\frac{d\varepsilon_1'}{d\lambda}} n_m. \tag{53}$$

The width w is not influenced directly by the shape factor, as can be seen from the way it was derived, (49)—(51). The changed resonance condition results in shift of of the peak wavelength into near infrared region (see plot of permittivity in Fig. 21). In this region, the imaginary part of the permittivity is considerably smaller than in the visible range. This leads to narrowing of the extinction peak and further improvement in the figure of merit, eq. (52).

To explore these effects numerically, the extinction spectra of spheroidal particles of different sizes, aspect ratios and RI of medium have been computed using the FDTD method. From these spectra, the bulk RI sensitivity S_B, width w and the figure of merit for bulk sensitivity χ_B was obtained. These results are in Table 3 and Figure 11.

The polarization of the incident light was along the longer axis of the particles and the particles were oriented with their longer axis perpendicular to the wave-vector.
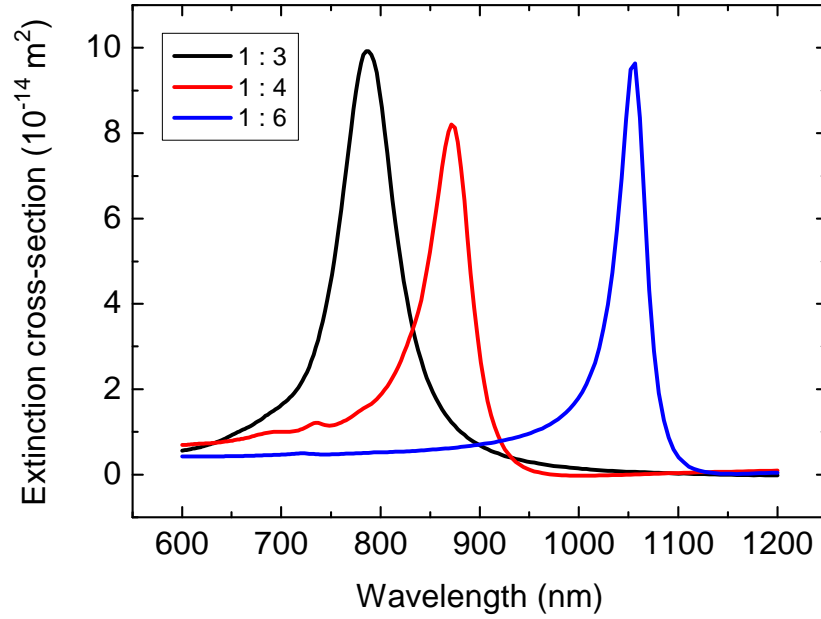
Figure 11: Extinction spectra of spheroidal gold particles of different aspect ratios and constant length (80 nm). Computed by FDTD.

Size (nm)	Aspect ratio	Bulk sens. S_B	Peak width w	FoM $\chi = S_B / w$
Aspect ratio dependence:				
140×47	1 : 3	449	67	6.7
140×35	1 : 4	442	52	8.5
140×23	1 : 6	595	35	17.0
Size dependence:				
80×20	1 : 4	317	18	17.6
140×35	1 : 4	442	52	8.5
200×50	1 : 4	487	100	4.9

Table 3: Bulk sensitivity, peak width and figure of merit for gold spheroidal particles of different sizes and aspect ratios. "Size" is length × width. Data computed by FDTD.

In this orientation, the electric field of the incident wave changes in the direction of one of the two smaller axis. The 80×20 and 140×23 nm particles are then in the region of applicability of the electrostatic approximation. Comparing results for these particles with electrostatic results for spherical particles, the prediction given by Equation (53) is confirmed: the bulk RI sensitivity is 6 times higher for highly elongated (1:6) particles than for spheres.

Some trends can be observed from Table 3. With a fixed particle length and increasing aspect ratio, the peak wavelength redshifts, the sensitivity increases and peak width decreases (due to decreasing imaginary part of metal permittivity). This results in three-fold increase in the figure of merit upon changing the aspect ratio from 1 : 3 to 1 : 6.

With a fixed aspect ratio and increasing particle size, the sensitivity increases, but the peak width increases more quickly. Upon increasing the particle length from 80 to 200 nm the figure of merit decreases more than three times.

These results agree with experimental observations by Chen et al. [25] who achieved bulk refractive index sensitivity of 366 nm/RIU using gold nanorods with an aspect ratio of 5.2. The peaks in this work suffered significant inhomogeneous broadening (~100 nm width), which decreases the figure merit.

3.2.6 Comparison of LSPR and planar SPR sensors

A theoretical comparison of bulk RI sensitivity, surface RI sensitivity and their corresponding figures of merit for LSP sensors with spherical particles of 80 nm diameter (Mie theory) and spheroidal particles of 80×20 nm (length $\times$ width) (FDTD) with SPR sensors with prism and grating couplers presented in Table 4.

	Bulk: S_B (nm/RIU)	Surface: S_S (nm/RIU) 10 nm layer	Line width w (nm)	FoM bulk: $\chi = S_B / w$	FoM surf.: $\chi = S_S / w$	Penetration depth (nm)*
Au spherical, 80 nm diameter	160	70	100	1.6	0.7	10
Au spheroidal, 80 x 20 nm	320	–	18	18	~8**	–
prism-coupled SPR, 750 nm ***	5000	350	60	80	5.8	200
grating-coupled SPR, 750 nm***	640	45	8	80	5.6	200

Table 4: Comparison of performance related parameters of SPR and LSP sensors. *For LSP, the penetration depth is defined as the thickness of the layer at which the surface sensitivity is half of the bulk RI sensitivity. For SPR, it is defined as the distance from the interface at which the electric field intensity drops to 1/e. **Estimated under the assumption that the ratio of S_S for spheroid to spherical is the same as this ratio for S_B. ***Data taken from [20].

In terms of figure of merit for bulk RI sensitivity, a LSP sensor based on spherical particles is clearly outperformed by conventional SPR sensors by a factor of 50, while a LSP sensor based on spheroidal particles only by a factor of 4.

Regarding the figure of merit for surface RI sensitivity, a spherical particle LSP sensor still performs about 10 times worse; but the performance of a spheroidal particle based LSP sensor is comparable to that of conventional SPR sensors.

Taking into account that advanced nanostructures with improved sensitivity [26, 43] and peak width [44] have been proposed, LSP sensors have the potential to be equal or better than SPR sensors in terms of performance characteristics.

4 Experimental

In this Chapter, gold spherical nanoparticles in liquid solutions are studied by means of transmission spectroscopy. The shift of the nanoparticle transmission dip due to changes in refractive index profile of its dielectric environment is experimentally demonstrated.

4.1 Materials

The samples were obtained from Nanocs, Inc (New York, USA), product codes GNB30 and GNB50. They were spherical gold nanoparticles of diameter 30 and 50 nm in aqueous solution, coated with a polymer layer to prevent aggregation and labeled with biotin, about 6 biotin molecules per particle, according to the manufacturers datasheet.

4.2 Experimental setup

Properties of the samples and their changes due to changes in their dielectric environment were characterized by means of transmission spectroscopy. The transmission spectra were measured on a setup depicted in Figure 12. Light from a halogen lamp (CLH500, Zeiss, Germany) is coupled into a multimode optical fiber (100 μm core diameter). The optical fiber illuminates a collimator, which creates a parallel beam. The beam is incident on micro-cuvette (Starna, USA) with 10 mm pathlength and 2×5 mm optical window (100 μl volume), containing the liquid sample. The transmitted light is coupled into a collecting optical fiber (400 μm core diameter) using a GRIN lens (2 mm diameter) and brought into a spectrometer (MCS501 fiber spectrometer, Zeiss, Germany), which is connected to a PC.
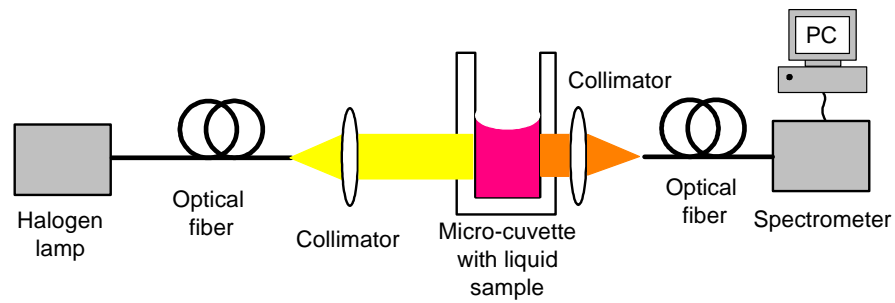
Figure 12: A schematic of the experimental setup for measuring transmission spectra.

The light source was left to stabilize for two hours. The samples in the cuvette were changed in-place, without removing the cuvette from its mount, to prevent problems with referencing. Between the measurements, the cuvette was repeatedly flushed with deionized water and dried by compressed air.

The collecting optical fiber with GRIN lens was placed close to the micro-cuvette (5 mm) to minimize the influence of sample inhomogenities on the beam and its spectral composition.

All displayed spectra have been divided by the transmission spectrum of their corresponding reference. A reference spectrum was measured after each sample.

The positions of the transmission dip were determined by fitting a third degree polynomial to the dip (half of the dip's depth was used) and taking the minimum of this polynomial as the dip position.

4.3   Transmission spectra and comparison with Mie theory

The transmission spectra of the solutions of 30 and 50 nm particles were measured with integration time of 350 ms and each displayed spectra was obtained by averaging 170 spectra for a total time of 60 s. As a reference, the transmission spectrum of deionized water was used. Results are shown in Figure 13 and Figure 14.
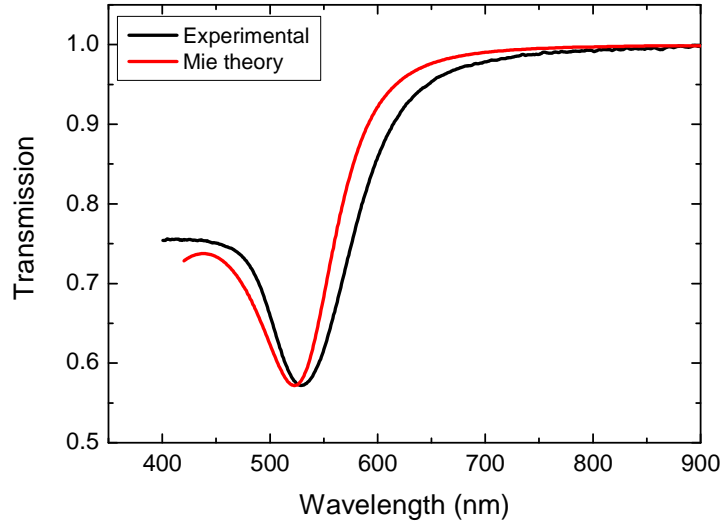
Figure 13: Comparison of transmission spectra as measured for the 30 nm particle samples (Experimental) and as computed by the Mie theory.
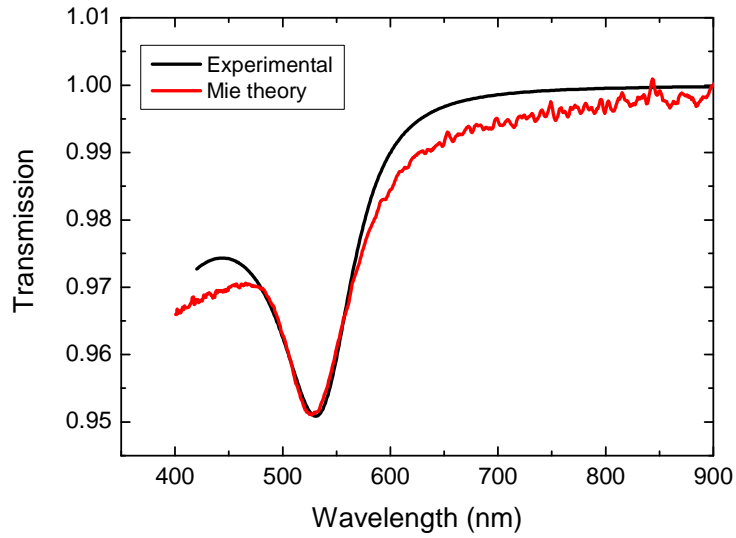
Figure 14: Comparison of transmission spectra as measured for the 50 nm particle samples (Experimental) and as computed by the Mie theory.

The transmission spectrum were also computed by the Mie theory. The transmission spectrum of a nanoparticle solution can be obtained from the extinction spectrum using [16]

$$T(\lambda) = \mathrm{e}^{-ndC_{\mathrm{ext}}(\lambda)} \qquad (54)$$

where T is transmission, n numeric concentration of the particles, C_{ext} extinction cross-section of a particle, d the light pathlength. C_{ext} has been determined by eq.

(22). Comparison of measured and computed transmission spectra for 30 nm gold particles can be seen in Figure 13 and Figure 14.

Since the concentration of the samples was not known exactly, n was determined to result in the same transmission at the dip minimum as in the experimental spectrum. Specifically, $n = 4.2 \times 10^{16}$ particles/m^3 for 30 nm particles and $n = 7.2 \times 10^{14}$ particles/m^3 for 50 nm particles. Because of this free parameter, we can only compare with experiment the relative value of C_{ext} and not its absolute value.

For 30 nm particles, the shape of the transmission spectrum is described well by the Mie theory using the permittivity model of gold shown in the Appendix. The dip position differs by 6 nm. This difference is caused by the permittivity model, as the properties of the nanoparticle gold might be different from those of bulk gold for which the experimental data on which the model is based were measured. Another reason could be the dispersion in size of the particles.

The same conclusions apply to the 50 nm nanoparticles. The off-dip parts of the experimental spectrum probably show extinction by unknown species present in the sample. Unfortunately, the 50 nm samples also suffered from significant aggregation of the colloid particles before the measurement was made, which resulted in low free nanoparticle concentration and consequently very weak extinction (< 3 % dip in transmission).

4.4 Sensitivity of dip position to medium refractive index

In this measurement, the bulk RI sensitivity S_B of the transmission dip will be determined. For this, the position of the transmission dip for nanoparticle samples in solutions of different refractive index was measured.

To change the RI of the solution in which the particles are immersed, the samples have been diluted by a series of water solutions of diethylene glycol (DEG) (Sigma-Aldrich, USA) of increasing concentrations. 50 μl of the undiluted sample (GNB30, GNB50) was mixed with 200 μl of a DEG solution. The DEG concentrations were selected to yield concentrations of 0 %, 20 %, 40 % and 60 % (volume fraction) of DEG in the final nanoparticle solution. The RI of the DEG solutions was measured on refractometer DSR-λ (Schmidt+Haensch, Germany). The RI of DEG was determined to be 1.4453 at 500 nm. As a reference, the transmission spectra of DEG solutions of said concentrations were used.

Diethylene glycol (DEG) was selected to simulate appropriate changes in solution RI. High viscosity of DEG, however, caused problems with sample homogeneity. To obtain maximum homogenity, the samples were

1. shaked on a laboratory shaker,

2. let stand for an hour to homogenize by diffusion,

3. after injection into the cuvette, they were allowed 15 minutes to settle down

To minimize the influence of residual inhomogeneity, the GRIN lens on the collecting fiber was selected instead of an ordinary lens for its larger acceptance angle, which results in lower sensitivity to beam angular deviation.

The transmission spectra were measured with integration time of 350 ms and each displayed spectra was obtained by averaging 170 spectra for a total time of 60 s.

In Figure 15 and Figure 17 it is shown how the transmission spectra change with changing refractive index of the solution. In Figure 16 (B) and Figure 18 (B) the positions of transmission dips have been plotted against the refractive index of solution. These positions were obtained by fitting the dip by a third degree polynomial and taking the minimum of this polynomial as the dip position. For fitting, only the portion of the dip from its minimum to half the dip's depth was used.
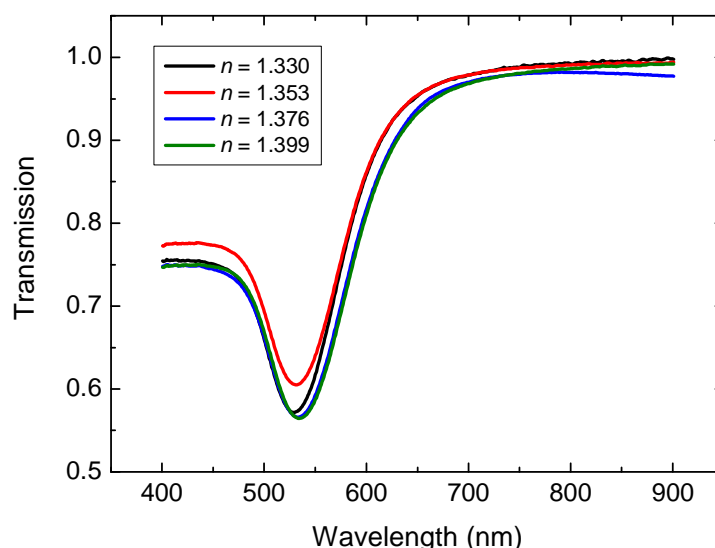
Figure 15: Transmission spectra of 30 nm particles in solutions of different RIs.
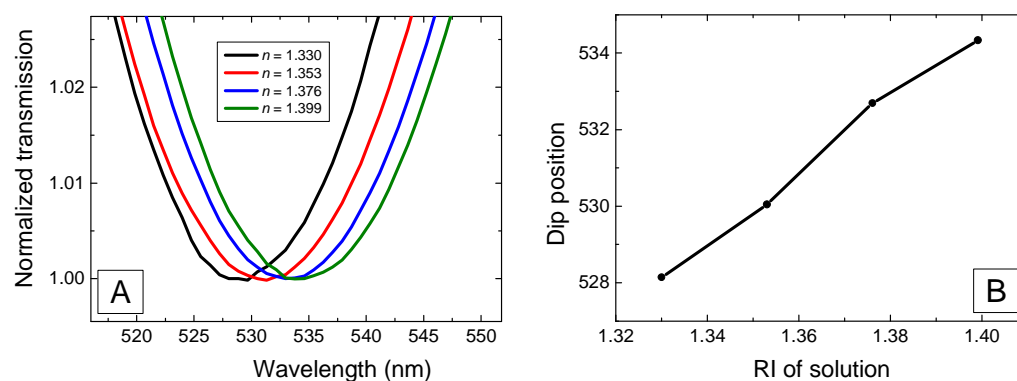
Figure 16: A: Transmission spectra of 30 nm particles in solutions of different RIs normalized to have the same minimum value, showing the shift of the peak with

Figure 17: Transmission spectra of 50 nm particles in solutions of different RIs.
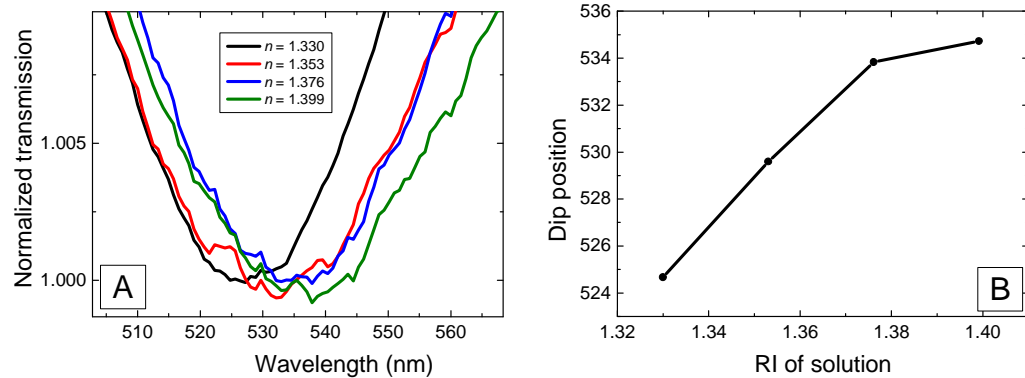
Figure 18: A: Transmission spectra of 50 nm particles in solutions of different RIs normalized to have the same minimum value, showing the shift of the peak with RI. B: Dependence of transmission dip position on solution RI. The line is a guide to the eye only.

The bulk RI sensitivity S_B has been estimated by linear fit of the dip position dependence on solution RI:

30 nm diameter particles: $S_B = (92 \pm 6)$ nm/RIU (Mie theory: 93 nm/RIU)

50 nm diameter particles: $S_B = (150 \pm 30)$ nm/RIU (Mie theory: 114 nm/RIU)

(the errors here are determined by the linear fit).

The value of bulk RI sensitivity for 30 nm particles is in good agreement with the prediction by Mie theory. For 50 nm particles, the agreement is much worse, which

is caused mainly by the very low concentration of free particles in the samples. This resulted in the transmission dip being very shallow. Then, any influence that contributes a slope to the spectrum can shift the apparent position of the peak significantly. These include extinction caused by other species in the sample (which couldn't be accounted for by referencing) and the fact that due to residual inhomogeneity, the sample formed a gradient of refractive index and bent the beam. The beam shift resulted in change of overall intensity (Figure 17). Because of RI dispersion (chromatic aberration), this can also resulted in spectral change. This is visible for the 50 nm particle samples

4.5   Sensitivity of dip position to presence of a biomolecular layer

In this measurement, the sensitivity of the nanoparticle transmission dip to changes in the RI of a thin surface layer is demonstrated. Specifically, it is shown that nanoparticles can be used to detect the presence of streptavidin molecules in solution. The GNB30 nanoparticles are functionalized (labeled) by biotin molecules. Streptavidin and biotin are known for their high mutual affinity and create a very strong bond, one of the strongest non-covalent bonds [45]. After adding streptavidin molecules to a solution of biotin-functionalized nanoparticles, streptavidin is expected to bind to the particles via biotin and increase the average RI in a layer on the particle's surface.

The transmission spectrum was monitored continuously in this experiment. The spectra were measured with 350 ms integration time and with averaging of 15 spectra, for a total measurement time of 5 s per one spectrum. These spectra were continuously loaded by a Matlab program created for this purpose, which processed them by dividing them by a reference spectrum (the transmission spectrum of deionized water) and fitting a third degree polynomial to the transmission dip to find the dip's wavelength and depth.

A solution of streptavidin (Sigma-Aldrich, USA) in water in a concentration of 0.5 μg/ml was prepared. After starting the acquisition of transmission spectra, 200 μl of the streptavidin solution was added into 50 μl of 30 nm particles solution (as received, not diluted) and immediately after that, 200 μl of the resulting solution was injected into the micro-cuvette.

Three experiments were performed. In the first two experiments, streptavidin was added to the nanoparticle solution as described above. To show that the change in dip position is due to the presence of streptavidin, a control experiment was run where the nanoparticle solution was only diluted by 200 μl of deionized water and 200 μl of the resulting solution was injected into the micro-cuvette.

The dependence of the dip wavelength on time is shown in Figure 19.
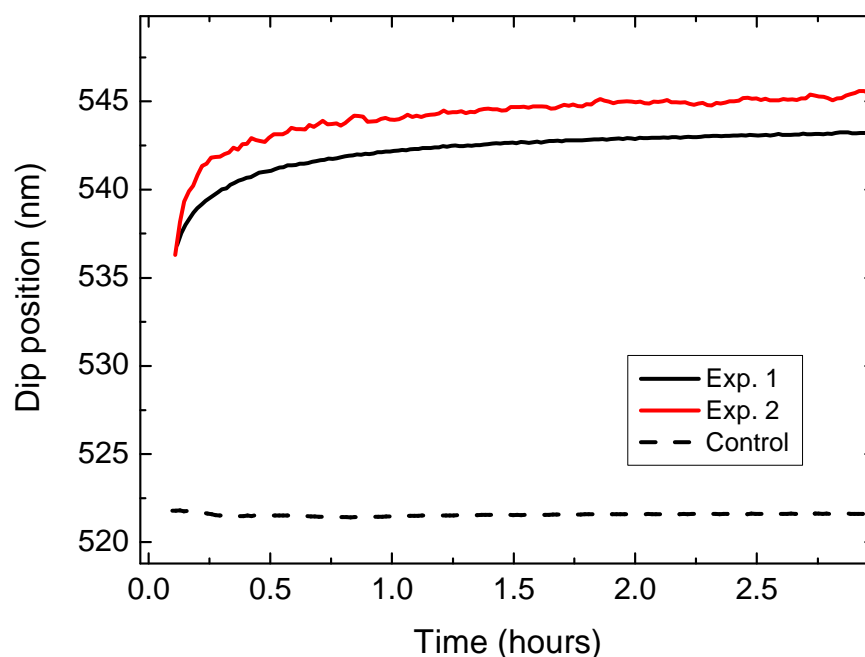
Figure 19: Detection of streptavidin by 30 nm particles – dependence of the position of the transmission dip on time. Two identical experiments have been made (Exp. 1 and Exp. 2) and a control experiment (Control) with no streptavidin. The shift of the dip shows the binding of streptavidin onto the particles.

In the first hour we observe a redshift of the minimum transmission of about 6—8 nm which is caused by binding of streptavidin molecules to the particle surface.

It can be seen in figure Figure 19 that the starting dip positions in experiments 1 and 2, when compared to the control experiment, differ by 10 nm. This was possibly caused by Rayleigh scattering on streptavidin molecules, which contributed a slope to the spectrum resulting in an apparent shift of the transmission dip.

Since four biotin molecules can bind to one streptavidin molecule, streptavidin can interlink the nanoparticles and thus induce aggregation. The aggregation is manifested by decrease of free nanoparticle concentration and consequently the shallowing of the transmission dip. This effect can be observed in Figure 20, where the depth of the transmission dip (i.e. transmission at the minimum) is plotted against time. After 4 hours, the colloid began to aggregate and after 12 hours, there was nearly no colloid left in the solution. This was not the case for the control experiment. From the dependence of dip depth on time it can be seen that the majority of the dip wavelength shift occurred before any major changes in concentration. This shows that the shift in the wavelength was not due to these changes, which could have influenced the apparent position of the dip.
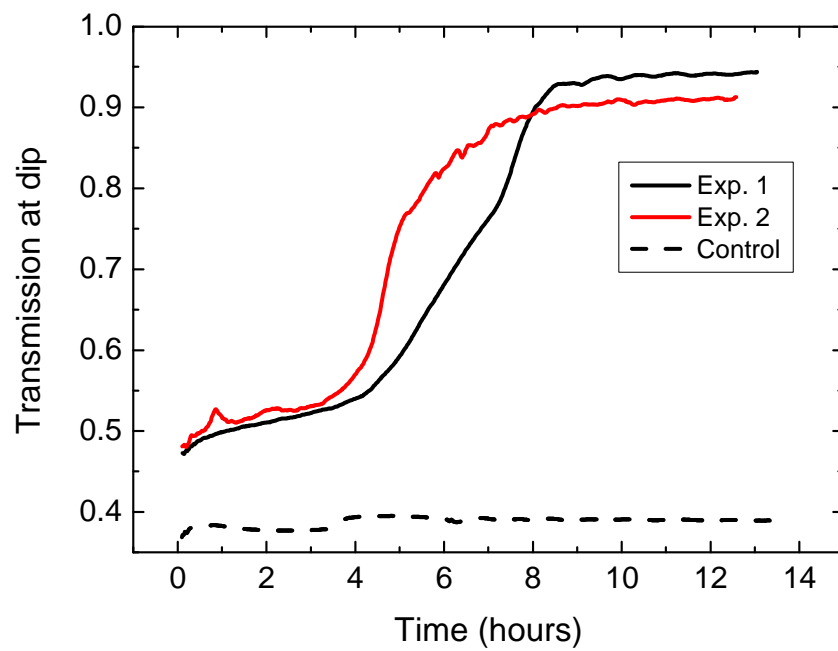
Figure 20: Detection of streptavidin by 30 nm particles – dependence of the depth of the transmission dip on time. Two identical experiments have been made (Exp. 1 and Exp. 2) and a control experiment (Control) with no streptavidin. The increase in transmission after 4 hours corresponds to aggregation of the particles.

5 Conclusions

The phenomenon of Localized Surface Plasmons on metallic nanoparticles and their optical excitation has been studied both theoretically and experimentally. Several theoretical approaches to analysis of localized surface plasmons and interaction of light with nanoparticles have been described. Spectral features of light interacting with the nanoparticle were studied. Special attention was given to analysis of sensitivity of these features to refractive index changes occurring at the surface or throughout the whole medium surrounding the nanoparticle and to width of the features. Both play an important role with respect to nanoparticles with LSP being used as a sensing platform.

Using the electrostatic approximation, simple formulae showing the major factors influencing these parameters have been derived. Using the Mie theory, the FDTD method and the DDA method, the above mentioned parameters have been numerically computed for a range a particle sizes and sensing layer thicknesses. It was concluded that for sensing applications involving the use of layers less than 10 nm thick, 10 nm particle diameter is the best choice. For systems with thicker layers, particles in diameter range 80—100 nm have been found optimal. Finally, it was demonstrated that by using non-spherical particles of high aspect ratios a further (ten-fold increase) in the figure of merit can be achieved.

In the experimental part of the work, a procedure and a laboratory setup for measuring transmission spectra of liquid nanoparticle samples, along with associated data acquisition and analysis software was developed. This allowed comparison of the shape and position of the transmission spectra and theoretical predictions of Mie theory. Both were found to be in good agreement. Furthermore, experimental value of the bulk refractive index sensitivity was determined. For 30 nm diameter particles, it is in excellent agreement with theoretical prediction, yielding a value of 90 nm/RIU. Finally, it was demonstrated that adsorption of streptavidin molecules results in a shift of the transmission minimum of up to 6 nm.

Future work will be aimed toward further exploration of non-spherical metallic particles and, especially, toward the understanding of ordered metallic arrays and nanostructures. The complex interplay of localized surface plasmons and light offers numerous fascinating opportunities for further research in this direction.

6   References

1.   Zhang, L.M. and D. Uttamchandani, *Optical Chemical Sensing Employing Surface-Plasmon Resonance.* Electronics Letters, 1988. **24**(23): p. 1469-1470.

2.   Slavik, R., J. Homola, and J. Ctyroky, *Single-mode optical fiber surface plasmon resonance sensor.* Sensors and Actuators B-Chemical, 1999. **54**(1-2): p. 74-79.

3.   Jory, M.J., P.S. Vukusic, and J.R. Sambles, *Development of a Prototype Gas Sensor Using Surface-Plasmon Resonance on Gratings.* Sensors and Actuators B-Chemical, 1994. **17**(3): p. 203-209.

4.   Day, Y.S.N., et al., *Direct comparison of binding equilibrium, thermodynamic, and rate constants determined by surface- and solution-based biophysical methods.* Protein Science, 2002. **11**(5): p. 1017-1025.

5.   Sakai, G., et al., *A surface plasmon resonance-based immunosensor for highly sensitive detection of morphine.* Sensors and Actuators B-Chemical, 1998. **49**(1-2): p. 5-12.

6.   Homola, J., *Surface Plasmon Resonance Sensors for Detection of Chemical and Biological Species.* Chemical Reviews B, 2008. **108**(2): p. 462-493.

7.   Harris, R.D., et al., *Integrated optical surface plasmon resonance immunoprobe for simazine detection.* Biosensors & Bioelectronics, 1999. **14**(4): p. 377-386.

8.   Mullett, W., E.P.C. Lai, and J.M. Yeung, *Immunoassay of fumonisins by a surface plasmon resonance biosensor.* Analytical Biochemistry, 1998. **258**(2): p. 161-167.

9.   Boardman, A.D., *Electromagnetic Surface Modes*. 1982, New York: Wiley-Interscience.

10. Maier, S.A. and H.A. Atwater, *Plasmonics: Localization and guiding of electromagnetic energy in metal/dielectric structures.* Journal of Applied Physics, 2005. **98**(1): p. -.

11. Atwater, H.A., *The promise of plasmonics.* Scientific American, 2007. **296**(4): p. 56-63.

12. Kahl, M., et al., *Periodically structured metallic substrates for SERS.* Sensors and Actuators B-Chemical, 1998. **51**(1-3): p. 285-291.

13. Fritzsche, W. and T.A. Taton, *Metal nanoparticles as labels for heterogeneous, chip-based DNA detection.* Nanotechnology, 2003. **14**(12): p. R63-R73.

14. Nath, N. and A. Chilkoti, *Label-free biosensing by surface plasmon resonance of nanoparticles on glass: Optimization of nanoparticle size.* Analytical Chemistry, 2004. **76**(18): p. 5370-5378.

15. Aslan, K., et al., *Angular-ratiometric plasmon-resonance based light scattering for bioaffinity sensing.* Journal of the American Chemical Society, 2005. **127**(34): p. 12115-12121.

16. Bohren, C.F. and D.R. Huffman, *Absorption and scattering of light by small particles.* 1983, New York: Wiley. xiv, 530 p.

17. Malyarchuk, V., et al., *High performance plasmonic crystal sensor formed by soft nanoimprint lithography.* Optics Express, 2005. **13**(15): p. 5669-5675.

18. Haes, A.J. and R.P. Van Duyne, *A nanoscale optical biosensor: Sensitivity and selectivity of an approach based on the localized surface plasmon resonance spectroscopy of triangular silver nanoparticles.* Journal of the American Chemical Society, 2002. **124**(35): p. 10596-10604.

19. Homola, J., *Present and future of surface plasmon resonance biosensors.* Analytical and Bioanalytical Chemistry, 2003. **377**(3): p. 528-539.

20. Homola, J., *Surface plasmon resonance based sensors.* Springer series on chemical sensors and biosensors, 4. 2006, Berlin ; New York: Springer. xii, 251 p.

21. Riboh, J.C., et al., *A nanoscale optical biosensor: Real-time immunoassay in physiological buffer enabled by improved nanoparticle adhesion.* Journal of Physical Chemistry B, 2003. **107**(8): p. 1772-1780.

22. Marinakos, S.M., S.H. Chen, and A. Chilkoti, *Plasmonic detection of a model analyte in serum by a gold nanorod sensor.* Analytical Chemistry, 2007. **79**(14): p. 5278-5283.

23. Murphy, C.J., et al., *One-dimensional colloidal gold and silver nanostructures.* Inorganic Chemistry, 2006. **45**(19): p. 7544-7554.

24. Murphy, C.J., et al., *Chemical sensing and imaging with metallic nanorods.* Chemical Communications, 2008(5): p. 544-557.

25. Chen, C.D., et al., *Sensing capability of the localized surface plasmon resonance of gold nanorods.* Biosensors & Bioelectronics, 2007. **22**(6): p. 926-932.

26. Larsson, E.M., et al., *Sensing characteristics of NIR localized surface plasmon resonances in gold nanorings for application as ultrasensitive biosensors.* Nano Letters, 2007. **7**(5): p. 1256-1263.

27. Xu, H.X. and M. Kall, *Modeling the optical response of nanoparticle-based surface plasmon resonance sensors.* Sensors and Actuators B-Chemical, 2002. **87**(2): p. 244-249.

28. Lee, K.S. and M.A. El-Sayed, *Gold and silver nanoparticles in sensing and imaging: Sensitivity of plasmon response to size, shape, and metal composition.* Journal of Physical Chemistry B, 2006. **110**(39): p. 19220-19225.

29. Brolo, A.G., et al., *Surface plasmon sensor based on the enhanced light transmission through arrays of nanoholes in gold films.* Langmuir, 2004. **20**(12): p. 4813-4815.

30. Lesuffleur, A., et al., *Periodic nanohole arrays with shape-enhanced plasmon resonance as real-time biosensors.* Applied Physics Letters, 2007. **90**(24): p. -.

31. Kelly, K.L., et al., *The optical properties of metal nanoparticles: The influence of size, shape, and dielectric environment.* Journal of Physical Chemistry B, 2003. **107**(3): p. 668-677.

32. Sung, J., et al., *Nanoparticle spectroscopy: Plasmon coupling in finite-sized two-dimensional arrays of cylindrical silver nanoparticles.* Journal of Physical Chemistry C, 2008. **112**(11): p. 4091-4096.

33. McFarland, A.D. and R.P. Van Duyne, *Single silver nanoparticles as real-time optical sensors with zeptomole sensitivity.* Nano Letters, 2003. **3**(8): p. 1057-1062.

34. Mie, G., *Beiträge zur Optik trüber Medien, speziell kolloidaler Metallösungen.* Ann. Phys., 1908. **330**: p. 377-445.

35. Mätzler, C., *MATLAB Functions for Mie Scattering and Absorption.* 2002, Institut für Angewandte Physik, Bern, Switzerland.

36. Draine, B.T. and P.J. Flatau, *Discrete-Dipole Approximation for Scattering Calculations.* Journal of the Optical Society of America a-Optics Image Science and Vision, 1994. **11**(4): p. 1491-1499.

37. Draine, B.T., and Flatau, P.J., *User Guide to the Discrete Dipole Approximation Code DDSCAT 6.1.* 2004.

38. Taflove, A. and S.C. Hagness, *Computational electrodynamics : the finite-difference time-domain method.* 3rd ed. Artech House antennas and propagation library. 2005, Boston: Artech House. xxii, 1006 p.

39. Yee, K.S., *Numerical Solution of Initial Boundary Value Problems Involving Maxwells Equations in Isotropic Media.* Ieee Transactions on Antennas and Propagation, 1966. **14**(3): p. 302-&.

40. Lumerical, Inc., *FDTD Solutions v5.1.* http://www.lumerical.com

41. Berenger, J.P., *A Perfectly Matched Layer for the Absorption of Electromagnetic-Waves.* Journal of Computational Physics, 1994. **114**(2): p. 185-200.

42. Kvasnicka, P. and J. Homola, *Optical Sensors based on Spectroscopy of Localized Surface Plasmons on Metallic Nanoparticles: Sensitivity Considerations.* Biointerphases, 2008. To be published.

43. Enoch, S., R. Quidant, and G. Badenes, *Optical sensing based on plasmon coupling in nanoparticle arrays.* Optics Express, 2004. **12**(15): p. 3422-3427.

44. Hicks, E.M., et al., *Controlling plasmon line shapes through diffractive coupling in linear arrays of cylindrical nanoparticles fabricated by electron beam lithography.* Nano Letters, 2005. **5**(6): p. 1065-1070.

45. Voet, D. and J.G. Voet, *Biochemistry.* 2nd ed. 1995, New York: J. Wiley & Sons. xvii, 1361 p.

46. Lide, D.R., *CRC Handbook of Chemistry and Physics* 1998: CRC-Press.

47. *Optical constants database available from SOPRA SA, France at http://www.sopra-sa.com/index2.php?goto=dl&rub=4*

48. Born, M. and E. Wolf, *Principles of Optics.* 1997: Cambridge University Press.

7 Appendix

7.1 Gold permittivity model

In all numerical computations in this work, permittivity of gold is described by the model consisting of a Drude and a Lorentz term

$$\varepsilon(\omega) = \varepsilon_1 - \frac{\omega_P^2}{iv_C\omega + \omega^2} + \frac{\varepsilon_L\omega_0^2}{\omega_0^2 - 2i\delta_0\omega - \omega^2} \tag{55}$$

$\varepsilon_1 = 7.077,\ \omega_P = 1.391\cdot10^{16},\ v_C = 1.411\cdot10^7,\ \varepsilon_L = 2.323,\ \omega_0 = 4.635\cdot10^{15},\ \delta_0 = 9.267\cdot10^{14}$

A plot of this permittivity together with experimental data from [46] and [47] is shown in Fig. 21.
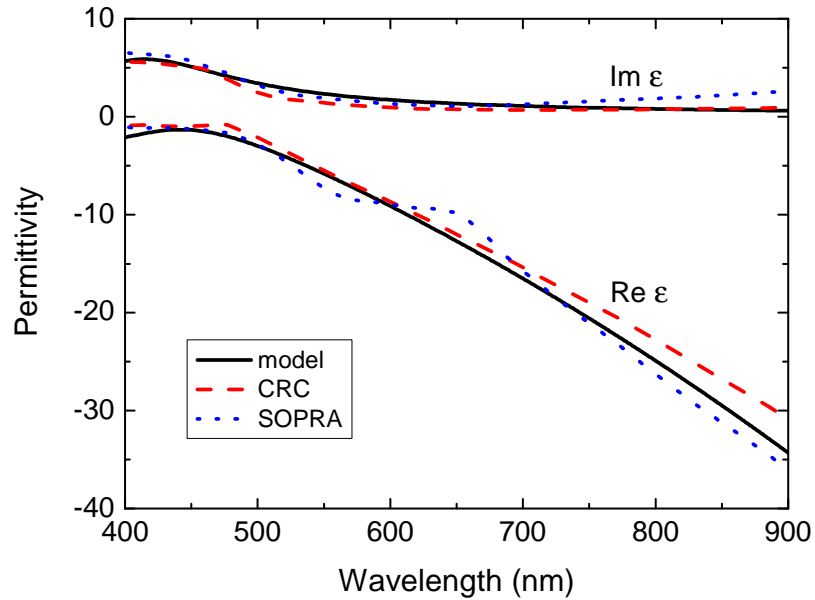
Fig. 21:. Permittivity of gold as a function of wavelegth. Theoretical model and experimental data from [46] (CRC) and [47] (SOPRA).

7.2 The program `mie.py`

This program implements the Mie theory as described in [48]. It requires the `scipy` scientific numerical library for the Python programming language.

```
#
# Implementation of the Mie theory
# Pavel Kvasnicka, 2007-04-11
#
# source: Born, Wolf: Principles of Optics
#

from scipy import *
# from numpy.oldnumeric import *  # for Python 2.4

lam = 550e-9  # default wavelength
nI  = 1.33
nII = 0.57 + 2.45j
a   = 15e-9  # particle radius

maxl = 20  # number of terms to sum
theta_samps = 15 # for numerical integration (includes endpoints)

c_light = 3e8

outname = 'extXlam20.dat' # outfile

# special functions
def psi(el,rho):
    return sqrt(pi*rho/2) * special.jv(el+0.5, rho)

def chi(el,rho):
    return -sqrt(pi*rho/2) * special.yv(el+0.5, rho)

def dzet1(el,rho):
    return psi(el,rho)-1j*chi(el,rho)

def psiD(el,rho):
    def psil(rrho): return psi(el,rrho)
    return derivative(psil, rho, dx=1e-5, order=5)

def dzet1D(el,rho):
    def dzet1l(rrho): return dzet1(el,rrho)
    return derivative(dzet1l, rho, dx=1e-5, order=5)

def legPm1(el,x): return special.lpmn(1,el,x)[0][1][el]
def legPm1D(el,x): return special.lpmn(1,el,x)[1][1][el]

# declare variables as global
omg=lamI=lamII=kI=kII=q=n=0.01
def dopocti_parametry():
    # compute other parameters
    global omg,lamI,lamII,kI,kII,q,n
    omg   = 2*pi*c_light/lam
    lamI  = lam/nI
    lamII = lam/nII
    kI    = omg/c_light*nI
    kII   = omg/c_light*nII
    q     = kI*a
    n     = nII/nI


elfaktor = ones(maxl+1,Complex)
def predpocitej_elfaktor():
    global elfaktor
    for el in range(1,maxl+1):
        elfaktor[el] = 1.j**(el+1) * (2.*el+1.)/(el*(el+1.))


eB = ones(maxl+1,Complex)
mB = ones(maxl+1,Complex)
def vypocti_koeficienty():
    global eB, mB
    for el in range(1,maxl+1):  # range() behaves as if #2 is not present!
        eB[el] = elfaktor[el] * (n*psiD(el,q)*psi(el,n*q) - psi(el,q)*psiD(el,n*q))
/ \
```

```python
                                        (n*dzet1D(el,q)*psi(el,n*q) -
dzet1(el,q)*psiD(el,n*q))

        mB[el] = elfaktor[el] * (n*psi(el,q)*psiD(el,n*q) - psiD(el,q)*psi(el,n*q))
/ \
                                        (n*dzet1(el,q)*psiD(el,n*q) -
dzet1D(el,q)*psi(el,n*q))


def ssin(x): # hack ;-)
    s = sin(x)
    if s != 0: return s
    else: return 0.0000000001

R1 = ones((maxl+1,theta_samps),Float)
R2 = ones((maxl+1,theta_samps),Float)    #maxl+1: index 0 zustava nevyuzity
def predpocitej_uhlovou_cast():
    global R1, R2
    d_th = pi/(theta_samps-1)  # jsou tam i krajni body!
    for el in range(1,maxl+1):
        th = 0.
        for i in range(theta_samps): # i = 0:theta_samps-1. theta_samps iteraci
            # hack:
            if th>pi*0.999999: th=th*0.99999
            # v pi totiz legPm1D diverguje, ale *sin ma konecnou limitu.
            # bohuzel numericky to nevychazi ;-)
            R1[el,i] = legPm1D(el,cos(th))*sin(th)
            R2[el,i] = legPm1(el,cos(th))*1/ssin(th)
            th = th + d_th
        # nakonec by melo byt th = pi + d_th.


def Qsca_integraci(print_integrand=0):
    "Vypocita Qsca pro aktualni parametry integracii vzdaleneho pole."
    integrand = ones(theta_samps,Float)
    osa_theta = ones(theta_samps,Float)
    d_th = pi/(theta_samps-1)
    th = 0.
    for i in range(theta_samps):
        th_slozka = 0.
        phi_slozka= 0.
        #print '(th=',th,')',
        for el in range(1,maxl+1):   # for el=1:maxl
            th_slozka += eB[el]*R1[el,i] - mB[el]*R2[el,i]
            phi_slozka += eB[el]*R2[el,i] - mB[el]*R1[el,i]
        integrand[i] = sin(th)*(th_slozka*conjugate(th_slozka) +
phi_slozka*conjugate(phi_slozka)).real
        osa_theta[i] = th
        th = th + d_th
    #
    Qs = integrate.simps(integrand,osa_theta) * 1/(a**2 * kI**2)
    if print_integrand: print 'integrand',integrand
    return Qs

def Qext_analyticky():
    "sig_ext podle B-W str. 661, eq (119)"
    sig_ext = 0.
    for el in range(1,maxl+1):
        sig_ext += (-1.j)**(el+1) * el*(el+1)*(eB[el] + mB[el])
    sig_ext = sig_ext.real;
    sig_ext = sig_ext*lamI**2 / (2*pi)
    return sig_ext/(pi*a**2)

def Qsca_analyticky():
    "sig_sca skoro podle B-W str. 661, eq (119) a podle toho pdfka..."\
    "\n tak ne... predelal jsem to vic na to pdfko :-)"
    sig_sca = 0.
    for el in range(1,maxl+1):
        delitel = 1.j**(el+1) * (2.*el+1.)/(el*(el+1.))
        sig_sca += (2*el+1)*(abs(eB[el]/delitel)**2 + abs(mB[el]/delitel)**2)
    sig_sca = sig_sca*lamI**2 / (2*pi)
    return sig_sca/(pi*a**2)



def zapis_xy_pole(jaky, kam):
    f = open(kam, 'w')
    for i in range(jaky.shape[0]):
        f.write(str(jaky[i][0])+'     '+str(jaky[i][1])+'\n')
    f.close()
```

```python
diel_fce = ones((200,3),Float)
#
def nacti_diel_fci(jmeno_souboru):
    global diel_fce
    #
    il = []   # index lomu
    f = open(jmeno_souboru,'r')
    lines = f.readlines()
    for l in lines:
        fields = l.split()          # Re n       Im n
        il += [[ float(fields[0])*1e-6, float(fields[1]), float(fields[2]) ]]   #
vnejsi zavorky se slejou s il
    diel_fce = array(il)

def interpoluj_il(pozad_lam):
    levy=-1   # libovolne
    pravy=-1
    for i in range(len(diel_fce[:,0])):
        if diel_fce[i,0] < pozad_lam:
            levy=i
        if diel_fce[i,0] > pozad_lam:
            pravy=i
            break #
    # mame oboji
    lev = diel_fce[levy]
    prav = diel_fce[pravy]
    return [lev[1] + (prav[1]-lev[1])*(pozad_lam-lev[0])/(prav[0]-lev[0]), \
            lev[2] + (prav[2]-lev[2])*(pozad_lam-lev[0])/(prav[0]-lev[0])]


# ****************************************************
# * Dependencies computation
# ****************************************************

def QextXlambda(lam_start, lam_step, num_steps):
    "napocita zavislost Qext vs. lambda do pole"
    #
    global lam
    global nII   # budeme menit z diel_fce
    res = ones((num_steps,2),Float)
    lam_local = lam_start;
    for i in range(num_steps):
        lam = lam_local # nastavime globalni
        il  = interpoluj_il(lam)
        nII = il[0] + il[1]*1j # nastavime globalni
        dopocti_parametry()
        vypocti_koeficienty()   # zmenilo se totiz q!
        res[i][0] = lam
        res[i][1] = Qext_analyticky()
        lam_local = lam_local + lam_step
        print '*',
    return res


def predpocty():
    predpocitej_uhlovou_cast()
    predpocitej_elfaktor()
    #
    dopocti_parametry()
    vypocti_koeficienty()


def main():
    global a
    global nI   # necessary

    nacti_diel_fci('au_radan.dat')
    nI=1.33
    for d in range(20,121,20):
        a = 0.5*d*1e-9 # polomer
        predpocty()
        QextXlambda_res = QextXlambda(lam_start=400e-9,lam_step=1.5e-9,num_steps=200)
        zapis_xy_pole(QextXlambda_res, 'au133_ext'+str(d)+'.dat')
        print d
    nI=1.38
    for d in range(20,121,20):
        a = 0.5*d*1e-9 # polomer
        predpocty()
        QextXlambda_res = QextXlambda(lam_start=400e-9,lam_step=1.5e-9,num_steps=200)
        zapis_xy_pole(QextXlambda_res, 'au138_ext'+str(d)+'.dat')
        print d
```

```python
        nacti_diel_fci('ag_palik.dat')
        nI=1.33
        for d in range(20,101,20):
            a = 0.5*d*1e-9 # polomer
            predpocty()
            QextXlambda_res = QextXlambda(lam_start=400e-9,lam_step=1.5e-9,num_steps=200)
            zapis_xy_pole(QextXlambda_res, 'ag133_ext'+str(d)+'.dat')
            print d
        nI=1.38
        for d in range(20,101,20):
            a = 0.5*d*1e-9 # polomer
            predpocty()
            QextXlambda_res = QextXlambda(lam_start=400e-9,lam_step=1.5e-9,num_steps=200)
            zapis_xy_pole(QextXlambda_res, 'ag138_ext'+str(d)+'.dat')
            print d

main()
```